Neuroscience Research
Available online: 26 November 2022
https://doi.org/10.1016/j.neures.2022.11.008

Preferential arborization of dendrites and axons of parvalbumin- and somatostatin-positive GABAergic neurons within subregions of the mouse claustrum

Megumu Takahashi[a,b,c,d], Tomoyo Kobayashi[b,c], Haruhi Mizuma[b,c], Kenta Yamauchi[b,c], Shinichiro Okamoto[b,c,e], Kazuki Okamoto[b,c], Yoko Ishida[b,c,e], Masato Koike[c,e], Masahiko Watanabe[f], Tadashi Isa[a,g], Hiroyuki Hioki[b.c.h,*]

[a]Department of Neuroscience, Graduate School of Medicine, Kyoto University, Kyoto, Kyoto 606-8501, Japan
[b]Department of Neuroanatomy, Juntendo University Graduate School of Medicine, Bunkyo-Ku, Tokyo 113-8421, Japan
[c]Department of Cell Biology and Neuroscience, Juntendo University Graduate School of Medicine, Bunkyo-Ku, Tokyo 113-8421, Japan
[d]Research Fellow of Japan Society for the Promotion of Science (JSPS), Chiyoda-ku, Tokyo 102-0083, Japan
[e]Advanced Research Institute for Health Sciences, Juntendo University, Bunkyo-Ku, Tokyo 113-8421, Japan
[f] Department of Anatomy, Faculty of Medicine, Hokkaido University, Sapporo, Hokkaido, 060-8638, Japan
[g]Institute for the Advanced Study of Human Biology (WPI-ASHBi), Kyoto University, Kyoto, Kyoto 606-8501, Japan
[h]Department of Multi-Scale Brain Structure Imaging, Juntendo University Graduate School of Medicine, Bunkyo-Ku, Tokyo 113-8421, Japan

[*]**Correspondence**: Hiroyuki Hioki, M.D., Ph.D., h-hioki@juntendo.ac.jp

Abstract

The claustrum coordinates the activities of individual cortical areas through abundant reciprocal connections with the cerebral cortex. Although these excitatory connections have been extensively investigated in three subregions of the claustrum—core region and dorsal and ventral shell regions—the contribution of GABAergic neurons to the circuitry in each subregion remains unclear. Here, we examined the distribution of GABAergic neurons and their dendritic and axonal arborizations in each subregion. Combining in situ hybridization with immunofluorescence histochemistry showed that approximately 10% of neuronal nuclei-positive cells expressed glutamic acid decarboxylase 67 mRNA across the claustral subregions. Approximately 20%, 30%, and 10% of GABAergic neurons were immunoreactive for parvalbumin (PV), somatostatin (SOM), and vasoactive intestinal polypeptide, respectively, in each subregion, and these neurochemical markers showed little overlap with each other. We then reconstructed PV and SOM neurons labeled with adeno-associated virus vectors. The dendrites and axons of PV and SOM neurons were preferentially localized to their respective subregions where their cell bodies were located. Furthermore, the axons were preferentially extended in a rostrocaudal direction, whereas the dendrites were relatively isotropic. The present findings suggest that claustral PV and SOM neurons might execute information processing separately within the core and shell regions.

Keywords

adeno-associated virus, claustrum subregion, Cre-lox recombination, GABAergic, local circuit, single-neuron reconstruction, tissue clearing

Introduction

The claustrum is a thin subcortical nucleus located between the insular cortex and the striatum. This small nucleus has abundant reciprocal excitatory connections with almost the entire cerebral cortex (Atlan et al., 2017; Wang et al., 2017; Zingg et al., 2018; Marriott et al., 2021; Shelton et al., 2022; Wang et al., 2022) and coordinates activity in the individual cortices (Crick and Koch, 2005; Smythies et al., 2012). Indeed, claustral neurons synchronously regulate cortical activity during slow-wave sleep in mice (Narikiyo et al., 2020) and reptiles (Norimoto et al., 2020). The excitatory connections between the claustrum and each cortical area have been further demonstrated to play key roles in various physiological functions (Goll et al., 2015; Chia et al., 2020), such as salience detection, attention, and regulation of impulsivity with claustro-frontocortical connections (White et al., 2018; Liu et al., 2019; Chia et al., 2020; Terem et al., 2020; Atlan et al., 2021); contextual memory with claustro-medial entorhinal cortical connections (Kitanishi and Matsuo, 2017); and motor response related to selection tasks with claustro-somatosensory cortical connections (Chevee et al., 2022).

The claustrum has been divided into three subregions by chemoarchitecture and cytoarchitecture (Binks et al., 2019). Parvalbumin (PV) immunoreactivity is higher in the central area of the claustrum—the core region—than in the surrounding area (Real et al., 2003; Davila et al., 2005), while the surroundings—the shell region—selectively display strong immunoreactivity for vesicular glutamate transporter 2 (VGluT2) (Real et al., 2006). Further, the central part of the claustrum shows a high density of neurons (Obst-Pernberg et al., 2001) and appears to correspond to the core region (Real et al., 2003). In addition, the shell region can be subdivided into ventral and dorsal parts by the extended boundary line between the dysgranular and agranular insular cortex (DI and AI) (Johnson et al., 2014; Binks et al., 2019). Although immunoreactivity for neuronal nuclei (NeuN) has been used to identify the claustrum (Kitanishi and Matsuo, 2017), the consistency of the core and shell subregional delineation based on PV and/or VGluT2 immunoreactivity (chemoarchitecture) and that based on cytoarchitecture is undetermined.

These three subregions—core region and dorsal and ventral shell regions—have distinct reciprocal connections with each cortical area. Anterograde and retrograde tracing studies have demonstrated reciprocal connections between the claustral subregions and cerebral cortex: claustral glutamatergic neurons in the core region send outputs to and receive inputs from the retrosplenial and visual cortices; those in the dorsal shell region connect with the motor and somatosensory cortices; and those in the ventral shell region have connections with the entorhinal cortex (Atlan et al., 2017; Marriott et al., 2021; Ham and Augustine, 2022; Shelton et al., 2022). This topographical organization suggests that the subregional structures would serve as functional modules via excitatory connections with the cerebral cortex (Chia et al., 2020; Smith et al., 2020; Marriott et al., 2021; Ham and Augustine, 2022).

GABAergic neurons in the claustrum have been characterized using immunohistochemical approaches (Eiden et al., 1990; Druga et al., 1993; Kowianski et al., 2001; Real et al., 2003; Davila et al., 2005; Kowianski et al., 2008). Electron microscopic observation demonstrated that claustral aspiny neurons as well as spiny neurons receive corticoclaustral synaptic inputs (LeVay and Sherk, 1981). An immunoelectron microscopic study also revealed that synaptic terminals immunopositive for GABA were often detected on the proximal dendrites and cell bodies of non-GABAergic neurons in the claustrum of tree shrew (Day-Brown et al., 2017). Among GABAergic neurons, PV-, somatostatin (SOM)-, and vasoactive intestinal polypeptide (VIP)-expressing neurons (PV, SOM, and VIP neurons) composed electrophysiologically distinct populations in the mouse claustrum (Graf et al., 2020). Moreover, PV neurons were reported to receive synaptic inputs from corticoclaustral axons and play an important role in amplification of selective corticoclaustral signals and in synchronization of claustral excitatory neurons (Kim et al., 2016; White et al., 2018). Despite the important role of GABAergic neurons in the claustrum circuitry, the distribution of GABAergic neurons within each subregion remains unclear. Furthermore, neurites immunopositive for PV and SOM are densely observed in the core and shell regions, respectively (Marriott et al., 2021), raising the question of whether the neurites of these two neurons are differentially distributed in the core and shell subregions.

In the present study, we performed triple immunofluorescence histochemistry for PV, VGluT2, and NeuN and delineated the mouse claustral subregions based on chemoarchitecture and cytoarchitecture. Subsequently, the populations of glutamatergic and GABAergic neurons were investigated by combining fluorescence in situ hybridization (FISH) and immunofluorescence histochemistry in each claustral subregion. We further quantified the distributions of PV, SOM, and VIP neurons in each subregion. Finally, we selectively visualized PV or SOM neurons by injecting recombinant AAV vectors into the claustrum of PV- or SOM-Cre knock-in mice and optically cleared 1-mm-thick brain slices. After acquisition of three-dimensional (3D) image stacks by confocal microscopy, we reconstructed and analyzed their dendrites and axons in the core and ventral shell regions at the single-neuron level.

Materials and methods

Animals

All procedures involving animals were performed in accordance with the National Institutes of Health Guide for the Care and Use of Laboratory Animals. The experiments were approved by the Institutional Animal Care and Use Committees of Juntendo University (Approval No: 2022148 and 2022149). All efforts were made to minimize animal suffering and the number of animals used.

Ten male C57BL/6J mice (8–12 weeks old; Nihon SLC), six male and female PV^{Cre} heterozygous mice (8–16 weeks old; $Pvalb^{tm1(cre)Arbr}$; The Jackson Laboratory Stock No: 008069) (Hippenmeyer et al., 2005), and ten male and female SOM^{Cre} heterozygous mice (8–16 weeks old; $Sst^{tm2.1(cre)Zjh}$; The Jackson Laboratory Stock No: 013044) (Taniguchi et al., 2011) were used in the present study. All mice were maintained in specific pathogen-free conditions under a 12/12 h light/dark cycle (light: 08:00–20:00) with ad libitum access to food and water.

Tissue preparation

Mice were deeply anesthetized with an intraperitoneal injection of sodium pentobarbital (200 mg/kg; Somnopentyl, Kyoritsu Seiyaku) and transcardially perfused with 20 mL of phosphate buffered 0.9% saline (PBS; pH 7.4) at 4°C, followed by the same volume of 4% paraformaldehyde (PFA; 1.04005.1000, Merck Millipore) in 0.1 M phosphate buffer (PB; pH 7.4). The mouse brains were removed and post-fixed in the same fixative overnight at 4°C. For triple or quadruple immunofluorescence labeling, the brains were cryoprotected in 30% (w/v) sucrose in 0.1 M PB and cut into 40-µm-thick coronal sections on a freezing microtome (SM2000 R, Leica Biosystems). For 3D reconstruction of PV and SOM neurons, the post-fixed brains were embedded in 2% agar (01028-85, Nacalai Tesque) in 0.1 M PB and cut into coronal slices of 1-mm thickness with a vibrating tissue slicer (Linear PRO7N, Dosaka EM). The sections and slices were stored in PBS containing 0.2% (w/v) NaN_3 at 4°C.

For ISH histochemistry, the mouse brains were post-fixed in the same fixative for 3 days at 4°C and cryoprotected in diethylpyrocarbonate (DEPC)-treated 30% (w/v) sucrose in 0.1 M PB. The brains were then cut into 30-µm-thick coronal sections on a freezing microtome and stored in an antifreeze solution that contained 30% (w/v) glycerol and 30% (w/v) ethylene glycol in DEPC-treated 0.1 M PB at –20°C until further use.

Immunofluorescence labeling

Triple or quadruple immunofluorescence labeling using free-floating sections was performed at 20–25°C, and all incubations were followed by a rinse with PBS containing 0.3% (v/v) Triton X-100 (35501-15, Nacalai Tesque) (PBS-X) for 10 min three times. The 40-µm-thick

sections were incubated overnight with the following mixture in PBS-X containing 0.12% (w/v) λ-carrageenan (035-09693; Sigma-Aldrich) and 1% (v/v) normal donkey serum (S30-100ML, Merck Millipore) (PBS-XCD): (i) 5 μg/mL affinity-purified mouse antibody against NeuN (MAB377, Merck Millipore, RRID:AB_2298772), 1/4,000-diluted rabbit antiserum against PV (PV-27, Swant, RRID:AB_2631173), and 1 μg/mL affinity-purified guinea pig antibody against VGluT2 (VGluT2-GP-Af810, Frontier Institute, RRID:AB_2571621); (ii) 5 μg/mL affinity-purified mouse antibody against NeuN, 1/4,000-diluted rabbit antiserum against PV, 1/50-diluted affinity-purified rat antibody against SOM-14 (MAB354, Merck Millipore, RRID:AB_2255365), and 1 μg/mL affinity-purified guinea pig antibody against VIP (Hioki et al., 2018). Subsequently, the sections were incubated for 2 h with the following mixture in PBS-XCD: (i) 5 μg/mL Alexa Fluor (AF) 488-conjugated goat antibody against mouse IgG (A-11029, Thermo Fisher Scientific, RRID:AB_2534088), 5 μg/mL AF568-conjugated goat antibody against rabbit IgG (A-11036, Thermo Fisher Scientific, RRID:AB_10563566), and 5 μg/mL AF647-conjugated goat antibody against guinea pig IgG (A-21450, Thermo Fisher Scientific, RRID:AB_2735091); (ii) 10 μg/mL CF405M-conjugated goat antibody against mouse IgG (20182, Biotium, RRID:AB_10557262), 5 μg/mL AF488-conjugated goat antibody against rabbit IgG (A-11034, Thermo Fisher Scientific, RRID:AB_2576217), 10 μg/mL AF568-conjugated goat antibody against rat IgG (A-11077, Thermo Fisher Scientific, RRID:AB_2534121), and 5 μg/mL AF647-conjugated goat antibody against guinea pig IgG. After the washes, the sections were re-fixed with 4% PFA in 0.1 M PB for 30 min, mounted onto 3-aminopropyltriethoxysilane (APS)-coated glass slides (Matsunami Glass), and coverslipped with 90% (v/v) glycerol and 2.5% (w/v) triethylenediamine (anti-fading reagent) in 20 mM Tris-HCl (pH 7.6).

Double or triple labeling with fluorescence in situ hybridization and immunofluorescence

Combination of single FISH and immunofluorescence labeling was performed as previously described (Hioki et al., 2010; Ma et al., 2011; Sohn et al., 2014) with some modification. Briefly, sense and antisense single-stranded riboprobes for *vesicular glutamate transporter 1* (*VGluT1*; nucleotides 855–1788 in GenBank accession No: XM_133432.2) (Nakamura et al., 2007) and *glutamic acid decarboxylase 67 kDa isoform* (*GAD67*; nucleotides 43–661 in GenBank accession No: Y12257.1) (Tamamaki et al., 2003) were synthesized with a digoxigenin (DIG) RNA labeling kit (1277073, Roche Diagnostics). Free-floating sections were treated with 1% (w/v) H_2O_2 in 0.1M PB for 30 min and then hybridized for 16–20 h at 60°C with 1 μg/mL DIG-labeled sense or antisense riboprobes in a hybridization buffer. After the washes and ribonuclease A treatment, the sections were incubated overnight at 20–25°C with one of the following mixtures: (i) 1/1,000- or 1/2,000-diluted peroxidase-conjugated sheep antibody against DIG (11-207-733-910, Roche Diagnostics, RRID:AB_514500) for *VGluT1* or *GAD67* and 5

μg/mL affinity-purified mouse antibody against NeuN; and (ii) 1/2,000-diluted peroxidase-conjugated sheep antibody against DIG, 5 μg/mL affinity-purified mouse antibody against NeuN, and either 1/4,000-diluted rabbit antiserum against PV, 5 μg/mL affinity-purified rabbit antibody against SOM-14 (T-4102, Peninsula Laboratories, RRID:AB_518613), or 1 μg/mL affinity-purified guinea-pig antibody against VIP. The sections were incubated for 30 min in a biotinylated tyramine (BT)-glucose oxidase (GO) reaction mixture containing 31 μM BT, 3 μg/mL GO, 20 μg/mL beta-D-glucose, and 1% (w/v) bovine serum albumin (BSA) in 0.1 M PB (Furuta et al., 2009; Kuramoto et al., 2009; Okamoto et al., 2021) to deposit BT onto the tissues via peroxidase activity. Subsequently, the sections were incubated for 2 h at 20–25°C with the following mixtures of secondary antibodies and streptavidin: 5 μg/mL AF488-conjugated streptavidin (S-11223, Thermo Fisher Scientific), 5 μg/mL AF568-conjugated donkey antibody against mouse IgG (A-10037, Thermo Fisher Scientific, RRID:AB_2534013), and AF647-conjugated goat antibody against rabbit IgG (A-21245, Thermo Fisher Scientific, RRID:AB_2535813) or AF647-conjugated goat antibody against guinea pig IgG. The sections were mounted onto APS-coated glass slides and coverslipped as described above.

Triple labeling with double fluorescence in situ hybridization and immunofluorescence

Combination of double FISH and immunofluorescence labeling was performed as previously described (Yamauchi et al., 2022b) with some modification. Briefly, sense and antisense single-stranded riboprobes for *GAD67* were synthesized with a fluorescein (FITC) RNA labeling kit (11-685-619-910, Roche Diagnostics). Free-floating sections were treated with 1% (w/v) H_2O_2 in 0.1M PB for 30 min and then hybridized for 16–20 h at 60°C with a mixture of 1 μg/mL DIG-labeled sense or antisense riboprobes for *VGluT1* and 1 μg/mL FITC-labeled sense or antisense riboprobes for *GAD67* in a hybridization buffer. After the washes and ribonuclease A treatment, the sections were incubated overnight at 20–25°C with 1/1,000-diluted peroxidase-conjugated sheep antibody against DIG. The sections were then incubated for 30 min in a fluorochromized tyramide (FT)-GO reaction mixture containing 10 μM CF488A tyramide (92171, Biotium), 3 μg/mL GO, 40 μg/mL beta-D-glucose, and 1% (w/v) BSA in 0.1 M PB. Subsequently, the sections were incubated overnight at 20–25°C with 2% (w/v) NaN_3 in 0.1M PB to inactivate the peroxidase activity. After the thorough washes, the sections were incubated overnight at 20–25°C with 1/1,000-diluted peroxidase-conjugated sheep antibody against FITC (11-426-346-910, Roche Diagnostics, RRID:AB_840257). The sections were then incubated for 30 min in an FT-GO reaction mixture containing 10 μM CF568 tyramide (92173, Biotium), 3 μg/mL GO, 40 μg/mL beta-D-glucose, and 1% (w/v) BSA in 0.1 M PB. Following the washes, the sections were incubated overnight at 20–25°C with 5 μg/mL affinity-purified mouse antibody against NeuN and then for 2 h with 5 μg/mL AF647-conjugated goat antibody against mouse IgG (A-21236,

Thermo Fisher Scientific, RRID:AB_2535805). The sections were mounted onto APS-coated glass slides and coverslipped as described above.

Confocal microscopy for tissue sections

The 3D image stacks of 30- and 40-μm-thick sections were acquired with a confocal laser scanning microscope (TCS SP8, Leica Microsystems) or a spinning disk confocal microscope (SDCM; Andor Dragonfly 201, Andor Technologies) built on an ECLIPSE FN1 upright microscope (Nikon Instruments). For TCS SP8, 16× multi-immersion (HC FLUOTAR 16x/0.60 IMM CORR VISIR, numerical aperture [NA] = 0.60, working distance [WD] = 2.5 mm; Leica Microsystems) and 25× water-immersion (HC FLUOTAR L 25x/0.95 W VISIR, NA = 0.95, WD = 2.50 mm; Leica Microsystems) objective lenses were used with the pinhole at 2–5.6 Airy disk unit and zoom factor at 1–1.2. CF405M, AF488 or CF488A, AF568 or CF568, and AF647 were excited by 405, 488, 552, and 638 nm lasers and observed through 420–500, 500–560, 570–650, or 650–700 nm emission prism windows, respectively, and detected with a z-interval of 2.5 μm per stack through a hybrid detector (Leica Microsystems). For Andor Dragonfly 201, a 20× water-immersion objective lens (CFI Apo LWD Lambda S 20XC WI, NA = 0.95, WD = 0.93 mm; Nikon Instruments) was used with the 40 μm pinhole and 1 × 1 or 3 × 3 binning. CF405M, AF488 or CF488A, AF568 or CF568, and AF647 were excited by 405, 488, 561, and 637 nm lasers, respectively, and observed through 445/46, 521/38, 594/43, and 698/77 nm emission filters, respectively, and detected with a z-interval of 2.5 μm per stack through a Zyla 4.2 PLUS sCMOS camera (Andor Technologies).

The image stacks were opened with Fiji/ImageJ (2.0.0-rc-69/1.52p) (Schindelin et al., 2012) and the Bio-Formats plugin (Linkert et al., 2010), and the number of cells in each channel was quantified using the Cell Counter plugin and the Image5D plugin. We counted the number of cells in the rostral (from +1.9 mm to +1.0 mm from the bregma), middle (+1.0 mm to 0 mm), and caudal (0 mm to –1.0 mm) parts of the claustrum. The global brightness and contrast of the images were adjusted with ImageJ and Canvas X Draw (ver 7.0.7, ACD systems).

Plasmid construction and AAV vector production

pAAV2-CMV-tTA-WPRE was constructed as follows. The oligonucleotides (P1 and P2/P3; Supplementary Table) were annealed to form double-stranded DNA and inserted into the MluI site and XhoI/BglII sites of pAAV-MCS (Stratagene; GenBank accession No: AF396260.1), respectively, resulting in pAAV-MCS2. The woodchuck hepatitis virus posttranscriptional regulatory element (WPRE; a gift from Dr. Hope TJ) (Zufferey et al., 1999) signal sequence was amplified using polymerase chain reaction (PCR; P4/P5) and inserted into the MluI/BglII sites of pAAV-MCS2, named as pAAV-MCSW2. We then amplified an improved version of

tetracycline-controlled transactivator (tTAad; Clontech) by PCR (P6/P7), inserted the product into the BamHI/XhoI sites of pAAV-MCSW2, and obtained the resultant vector—pAAV2-CMV-tTA-WPRE.

pAAV2-TRE-FLEX-palGFP-BGHpA was constructed as follows. The fragment, TRE-GFP-BGHpA, was excised from pTRE-GFP-BGHpA (Hioki et al., 2009) and inserted into the XhoI/NotI sites of pENTR™1A (Thermo Fisher Scientific), resulting in pENTR1A-TRE-GFP-BGHpA. The annealed oligonucleotide (P8/P9) containing BamHI-BglII-SalI restriction enzyme sites was inserted into the EcoRI/MluI sites of pENTR1A-TRE-GFP-BGHpA to replace the GFP sequence, resulting in pENTR1A-TRE-BBSM-BGHpA. The flip-excision (FLEX) switch sequence (Schnutgen et al., 2003), which contains two pairs of loxP and lox2272 sites in opposite orientations, was excised from pBSIISK-hFLEX (Sohn et al., 2017) and inserted into the BamHI/MluI sites of pENTR1A-TRE-BBSM-BGHpA. Then, the self-annealed oligonucleotide (P10) was successively inserted into both the BamHI and BglII sites of the plasmid to eliminate those restriction enzyme sites, resulting in pENTR1A-TRE-FLEX-BGHpA. The insert of the resultant entry vector, TRE-FLEX-BGHpA sequence, was transferred to the destination vector, pAAV2-DEST(f) (Sohn et al., 2017), by homologous recombination with LR Clonase II (11791020, Thermo Fisher Scientific) to generate pAAV2-TRE-FLEX-BGHpA. The annealed oligonucleotide (P11/P12) containing EcoRI-BglII-SalI-HindIII-BamHI restriction enzyme sites was inserted into the EcoRI/SalI sites of pAAV2-TRE-FLEX-BGHpA, resulting in pAAV2-TRE-FLEX-EBSHB-BGHpA. Finally, EGFP with a palmitoylation signal derived from the GAP-43 N-terminus (palGFP) (Moriyoshi et al., 1996; Tamamaki et al., 2000; Furuta et al., 2001; Sohn et al., 2017; Okamoto et al., 2020) was amplified with PCR (P13/P14) and inserted into the BamHI/SalI sites of pAAV2-TRE-FLEX-EBSHB-BGHpA, and the resultant vector was named as pAAV2-TRE-FLEX-palGFP-BGHpA.

AAV vector particles were produced and purified as previously described (Sohn et al., 2017; Takahashi et al., 2021). Briefly, pAAV2-TRE-FLEX-palGFP-BGHpA or pAAV2-CMV-tTA-WPRE and two helper plasmids, pBSIISK-R2C1 (Sohn et al., 2017) and pHelper (Stratagene; GenBank accession No: AF369965.1), were co-transfected into HEK293T cells (RCB2202, Riken BRC) using polyethylenimine (23966, Polysciences). Virus particles were purified from the cell lysate and supernatant using ultracentrifugation with OptiPrep (1893, Serumwerk Bernburg) and concentrated using ultrafiltration with Amicon® Ultra-15 (UFC903024, Merck Millipore). The physical titer of the AAV vector (genome copies [gc]/mL) was measured using quantitative PCR (P15/P16) with the purified virus solutions; 8.0×10^{13} gc/mL for AAV2/1-CMV-tTA-WPRE and 4.4×10^{14} gc/mL for AAV2/1-TRE-FLEX-palGFP-BGHpA. The solution was stored in aliquots at –80°C until further use.

Stereotaxic injection of AAV vectors

AAV vector injection into mouse brains was performed as previously described (Okamoto et al., 2020; Okamoto et al., 2021; Takahashi et al., 2021) with some modification. Briefly, mice were deeply anesthetized with an intraperitoneal injection of medetomidine (0.3 mg/kg; Domitor, Zenoaq), midazolam (4 mg/kg; Dormicum, Astellas Pharma), and butorphanol (5 mg/kg; Vetorphale, Meiji Seika Pharma) and placed in a stereotaxic apparatus (SR-5M1-HT, Narishige). A 0.2-μL volume of the virus solution mixture (AAV2/1-CMV-tTA-WPRE, 8.0×10^8 gc/mL; AAV2/1-TRE-FLEX-palGFP-BGHpA, 4.4×10^{14} gc/mL) was bilaterally injected into the claustrum of $PV^{+/Cre}$ or $SOM^{+/Cre}$ mice by pressure through a glass micropipette attached to Picospritzer III (Parker Hannifin). The injection coordinates were as follows: 1.1 mm anterior to the bregma, 3.1 mm lateral to the midline, and 2.5 mm ventral to the brain surface. The mice recovered from anesthesia with an intraperitoneal injection of atipamezole (1.5 mg/kg; Antisedan, Zenoaq) and were maintained under regular health check-ups for 7 to 10 days.

3D reconstruction of PV and SOM neurons in the claustrum

The 1-mm-thick brain slices were optically cleared with Sca*l*eSF treatment (Furuta et al., 2022; Yamauchi et al., 2022a; Yamauchi et al., 2022c). Briefly, the slices were incubated with Sca*l*eS0 solution for 2 h at 37°C, PBS(–) (27575-31, Nacalai Tesque) for 15 min at 20–25°C, and Sca*l*eS4 solution for 10 h at 37°C. The cleared slices were observed under an SDCM equipped with a 10× dry objective lens (CFI Plan Apo Lambda 10X, NA = 0.45, WD = 4.0 mm; Nikon Instruments). We checked whether brain slices contained the claustral neurons labeled with EGFP and selected 5 of 12 hemispheres from $PV^{+/Cre}$ mice and 8 of 20 hemispheres from $SOM^{+/Cre}$ mice for subsequent procedures. The formula for Sca*l*eS0 solution was 20% (w/v) D-(–)-sorbitol (06286-55, Nacalai Tesque), 5% (w/v) glycerol (G9012, Sigma-Aldrich), 1 mM methyl-β-cyclodextrin (M1356, Tokyo Chemical Industry), 1 mM γ-cyclodextrin (037-10643, Wako Pure Chemical Industries), and 3% (v/v) dimethyl sulfoxide (DMSO; 13407-45, Nacalai Tesque) in PBS(–) and that for Sca*l*eS4 solution was 40% (w/v) D-(–)-sorbitol, 10% (w/v) glycerol, 4 M urea (35940-65, Nacalai Tesque), 0.2% (w/v) Triton X-100, and 25% (v/v) DMSO in distilled deionized water (DDW) (Hama et al., 2015; Miyawaki et al., 2016).

We then performed immunofluorescence labeling using the AbSca*l*e method (Hama et al., 2015) on the brain slices. After treatment with 1% (w/v) H_2O_2 in PBS(–) for 1 h at 20–25°C, the slices were incubated with Sca*l*eA2 solution for 12 h, Sca*l*eB4(0) solution for 6 h, and Sca*l*eA2 solution for 3 h at 37°C. After washes with PBS(–), the slices were incubated with AbSca*l*e solution containing 5% P-RAN-GFP1 (horseradish peroxidase fused nanobody against EGFP) (Yamagata and Sanes, 2018) solution and 1% (v/v) normal donkey serum for 12 h at 4°C. After washes with AbSca*l*e solution and 0.1 M PB, the slices were incubated for 2 h at 20–25°C in an

FT-GO reaction mixture containing 10 μM CF488A tyramide, 3 μg/mL GO, 2% (w/v) BSA, and 20 μg/mL β-D-glucose in 0.1 M PB. After three washes with 0.1 M PB for 30 min at 20–25°C, the slices were incubated with AbSca*l*e solution containing 5 μg/mL affinity-purified rabbit antibody against NeuN (ABN78, Merck Millipore, RRID:AB_10807945) for 5 days at 37°C, followed by 1.5 μg/mL AF647-conjugated nanobody against rabbit IgG (SA5-10327, Thermo Fisher Scientific) for 1 day at 37°C. After washes with AbSca*l*e solution, the slices were re-fixed with 4% PFA in 0.1 M PB for 30 min at 20–25°C. Finally, the slices were optically cleared with Sca*l*eS4 solution for 2 h at 37°C. To keep the sizes of the cleared slices isometric with the original ones, the cleared slices were placed on the imaging chamber (Furuta et al., 2022; Yamauchi et al., 2022a; Yamauchi et al., 2022c) and embedded in 1.5% agarose (L03, Takara Bio) in Sca*l*eS4D25(0) solution (Sca*l*eS4 gel) (Hama et al., 2015). The formula for Sca*l*eA2 solution was 4 M urea, 0.1% (w/v) Triton X-100, and 10% (w/v) glycerol in DDW; that for Sca*l*eB4(0) solution was 8 M urea in DDW; that for AbSca*l*e solution was 0.33 M urea and 0.1% (w/v) Triton X-100 in PBS(–); and that for Sca*l*eS4D25(0) solution was 40% (w/v) D-(–)-sorbitol, 10% (w/v) glycerol, 4 M urea, and 25% (v/v) DMSO in DDW.

3D image stacks of the slices were acquired with an SDCM using a 20× glycerol-immersion objective lens (CFI 90 20×C Glyc, NA = 1.0, WD = 8.2 mm; Nikon Instruments), and with the 40 μm pinhole, 3 × 3 binning, and a z-interval of 2–2.5 μm. EGFP/CF488A and AF647 were excited by 488 and 637 nm lasers, observed through 521/38 and 698/77 nm emission filters, and detected using a Zyla 4.2 PLUS sCMOS camera. The image stacks were deconvoluted with a Fusion software (ver 2.3.0.45, Andor Technologies), and the 3D renderings were created with an Imaris software (ver 9.9.1, Bitplane).

The dendrites and axons of PV and SOM neurons were three-dimensionally reconstructed in 1–3 serial image stacks with a Neurolucida 360 software, a computer-assisted neuron tracing system (ver 2021.1.3, MBF Bioscience), as follows. Image stacks files were converted to JPEG 2000 file format with a MicroFile+ software (ver 2021.1.3, MBF Bioscience), and the image files were loaded onto Neurolucida 360. The neurites of PV and SOM neurons were then traced with an automatic or semi-automatic directional kernel algorithm in a 3D environment or with manual drawing in a two-dimensional (2D) environment. Among the neurites, the dendrites were distinguished from the axon, whose extensive ramifications maintained a constant diameter through the ends and possessed varicosities. Each subregion of the claustrum was manually delineated with reference to NeuN immunoreactivity in every 100-μm stack images.

After the 3D reconstruction of PV and SOM neurons, the morphological characteristics were quantitatively analyzed using the built-in functions of a Neurolucida Explorer software (ver 2021.1.1, MBF Bioscience). The dendritic and axonal lengths in each region were measured with

the “Closed surface analysis” function. Arborizations of dendrites and axons were three-dimensionally analyzed with the “Sholl analysis” function (3D Sholl analysis). The reconstructed data were projected along the rostrocaudal (RC), DV, and mediolateral (ML) directions with Neurolucida Explorer, referring to the mouse brain atlas (Paxinos and Franklin., 2007). The dendritic and axonal arborizations on each projected plane were analyzed using the "Sholl analysis” plugin (Ferreira et al., 2014) in Fiji/ImageJ (2D Sholl analysis). The data were analyzed and plotted with the pandas (McKinney et al., 2010), NumPy (Harris et al., 2020), and Matplotlib (Hunter, 2007) libraries in Python 3.7 (https://www.python.org/).

Statistical analysis

Data are represented as means ± standard deviations (SDs). Multiple statistical comparisons were performed for the data presented in Table 1 and Table 2 with Kruskal–Wallis tests followed by Dunn's post-hoc multiple comparison test. For the data in Fig. 7 and Fig. 8, analysis was performed with two-way analysis of variance (ANOVA) followed by Bonferroni’s post-hoc multiple comparison tests using a Prism8 software (ver 8.4.3, GraphPad Software).

Data availability

The datasets generated during and/or analyzed during the current study and all biological materials reported in this article are available from the corresponding author on reasonable request.

Results

Delineation of the mouse claustral subregions

In the present study, we utilized cytoarchitecture and chemoarchitecture to identify the claustrum and its subregions. We performed triple immunofluorescence histochemistry for NeuN, PV, and VGluT2 with mouse coronal sections (Fig. 1). Based on the density and size of NeuN-positive cells, the claustrum was distinguished from the adjacent layer Vb of the insular cortex as previously reported (Atlan et al., 2017; Binks et al., 2019; Ham and Augustine, 2022) and divided into two subregions: the core region with a high cell density and the shell region around the core region (Fig. 1A, B_1, C, D_1, E, F_1 and Fig. S1) (Obst-Pernberg et al., 2001; Real et al., 2003; Kitanishi and Matsuo, 2017). Further, the shell region was subdivided into the dorsal and ventral parts by the extended line of border between the DI and AI (Fig. 1A, C, E) (Smith and Alloway, 2010; Binks et al., 2019; Dillingham et al., 2019; Smith et al., 2019). Strong immunoreactivity for PV or VGluT2 was observed in the central or surrounding area, respectively (Fig. $1B_2$, B_3, D_2, D_3, F_2, F_3) (Real et al., 2003; Davila et al., 2005; Real et al., 2006; Binks et al., 2019). We confirmed that the core and shell regions distinguished with NeuN immunoreactivity (cytoarchitecture) matched the areas classified by PV and VGluT2 immunoreactivities (chemoarchitecture) on the present triple immunofluorescence staining (Fig. 1B, D, F). We thus employed NeuN immunoreactivity for the subsequent delineation of the claustrum.

The distribution of three subgroups of GABAergic neurons

The distribution of glutamatergic and GABAergic neurons in each subregion of the claustrum was explored with FISH histochemistry for VGluT1 or GAD67 mRNA combined with immunofluorescence histochemistry for NeuN (Fig. 2). VGluT1-expressing cells accounted for 91.9%, 90.0%, and 87.3% of NeuN-positive cells in the core region and dorsal and ventral shell regions, respectively (Fig. $2A_1$–B_3), while GAD67-expressing cells constituted 9.1%, 9.3%, and 11.2% in these subregions (Fig. $2C_1$–D_3), respectively. Further, no colocalization was found between the signals for VGluT1 and GAD67 mRNAs (no GAD67-expressing cell in 3483 VGluT1-expressing cells; noVGluT1-expressing cell in 344 GAD67-expressing cells; Fig. S2). Although the proportion of GAD67-expressing neurons in the rostral core region was significantly lower than that in the rostral shell region, VGluT1- and GAD67-expressing neurons were almost homogeneously located throughout the claustral subregions (Table 1).

We then investigated the proportion of PV, SOM, and VIP neurons by combining FISH histochemistry for GAD67 mRNA with double immunofluorescence histochemistry for NeuN and one of the neurochemical markers (Fig. 3). PV neurons consisted of 26.2%, 17.1%, and 20.0% of GAD67-expressing neurons in the core region and dorsal and ventral shell regions, respectively. PV neurons were more abundant in the core region, and a statistically significant difference was

detected between the core and dorsal shell regions (Fig. 3A–B_3, Table 2). SOM neurons occupied 30.2%, 26.9%, and 32.1% of GABAergic neurons in the core region and dorsal and ventral shell regions, respectively, and appeared uniformly distributed throughout the claustrum (Fig. 3C–D_3; Table 2). VIP neurons showed no significant difference in the distribution across the claustral subregions, and 9.3%, 9.7%, and 8.7% of GABAergic neurons were immunoreactive for VIP in the core region and dorsal and ventral shell regions, respectively (Fig. 3E–F_3; Table 2). We also found that SOM neurons were most abundant in the dorsal and ventral shell regions, while the proportion of SOM neurons was not significantly different from that of PV neurons in the core region. Moreover, the VIP neuron population was smaller than those of the others throughout the claustrum ($p < 0.01$ for all pairs, except for $p = 0.11$ between PV and SOM neurons in the core region; two-way ANOVA followed by Bonferroni's multiple-comparison test; Table 2).

We further examined whether these three neurochemical markers would show overlap in claustral neurons using quadruple immunofluorescence labeling for NeuN, PV, SOM, and VIP (Fig. 4A_1–B_4). We found no colocalization between SOM and VIP or between PV and VIP immunoreactivities in the claustral neurons, although slight colocalization between PV and SOM immunoreactivities was observed (0.8–3.0% of SOM neurons in PV neurons; 0.5–3.0% of PV neurons in the SOM neurons; Table 3). These results indicate that PV, SOM, and VIP neurons constitute three distinct subgroups and collectively cover 62%, 52%, and 60% of GABAergic neurons in the core region and dorsal and ventral shell regions of the claustrum, respectively (Fig. 4C).

Restricted distribution of dendrites and axons of PV and SOM neurons in the core and ventral shell regions

Abundant neurites immunopositive for PV were observed in the core region, and those for SOM in the shell region (Fig. 4; Marriott et al., 2021). We analyzed the dendritic and axonal arborizations of PV and SOM neurons in the core and ventral shell regions to determine whether their neurite extension differ between the subregions. The mixture of diluted driver vector (AAV2/1-CMV-tTA-WPRE) and undiluted reporter vector (AAV2/1-TRE-FLEX-palGFP-BGHpA) (Fig. 5A) was injected into the claustrum of $PV^{+/Cre}$ or $SOM^{+/Cre}$ knock-in mice. After visualizing the dendrites and axons, optically cleared brain slices were observed with a confocal microscope to acquire 3D image stacks (Fig. 5B, C). We obtained 3 and 4 neurons in the core and ventral shell regions from 5 hemispheres of $PV^{+/Cre}$ mice (PV-core neurons, #1–3; PV-shell neurons, #4–7; Fig. 5D), and 3 and 5 neurons in the core and ventral shell regions from 8 hemispheres of $SOM^{+/Cre}$ mice (SOM-core neurons, #8–10; SOM-shell neurons, #11–15; Fig. 5D). We reconstructed the dendrites and axons and the claustral structures in 3D image stacks. PV-core #2, PV-shell #6, and PV-shell #7 neurons were derived from a single hemisphere. Although

the three neurons extended their neurites within the hemisphere, combining the 1-mm-thick brain slices with a tissue clearing method enabled us to trace their dendrites and axon of each neuron (Fig. S3A). The three neurons had few overlaps (Fig. S3B), and we separated them without including fibers of neighboring labeled neurons. The other 12 neurons were derived from the respective hemispheres, where a single EGFP-labeled neuron was found inside the claustrum and distinguished from other labeled neurons outside the claustrum (Fig. 6).

We then calculated the proportions of dendrite and axon lengths distributed in each region (Table 4). The fluorescence images of PV-core neurons showed that their neurites were mainly confined within the core region (Fig. $6A_1$). After 3D reconstruction of their neurites, we observed 99.1% of dendrites and 99.8% of axons inside the claustrum. The reconstructed neurites also showed that the arborization fields of dendrites slightly exceeded those of axons. Indeed, we found that 76.0% of all dendrites and 92.8% of all axons remained within the core region, while 23.0% and 7.0% extended to the dorsal and ventral shell regions, respectively (Fig. $6A_2$; Table 4). Similarly, in the fluorescence images of SOM-core neurons, their neurites appeared to be closely packed in the core region (Fig. $6B_1$). We observed that 95.7% and 94.6% of dendrites and axons formed arborizations inside the claustrum, respectively, and that 79.4% and 84.4% were located within the core region, respectively (Fig. $6B_2$; Table 4). These results indicate that the dendrites and axons of both PV-core and SOM-core neurons are mostly confined within the core region.

In contrast, the fluorescence images of PV-shell neurons showed that their neurites mainly existed in the dorsal and ventral shell regions and avoided sending axons to the core regions (Fig. $6C_1$). PV-shell neurons spread 79.0% of dendrites and 85.7% of axons inside the claustrum. We further found that 75.1% of dendrites and 73.6% of axons existed in the dorsal and ventral shell regions, while only 3.9% of dendrites and 12.1% of axons existed in the core region (Fig. $6C_2$; Table 4). SOM-shell neurons showed a similar tendency to PV-shell neurons. The neurites of SOM-shell neurons rarely entered the core region were localized in the dorsal and ventral shell regions (Fig. $6D_1$). We observed that 74.7% of dendrites and 64.8% of axons were located within the claustrum. Moreover, 72.5% of dendrites and 57.6% of axons were distributed in the dorsal and ventral shell regions, while only 2.5% of dendrites and 7.3% of axons resided in the core region (Fig. $6D_2$; Table 4). These results suggest that PV-shell and SOM-shell neurons spread their dendrites and axons in the shell region and infrequently enter the core region.

Almost all neurites of PV-core and SOM-core neurons were detected inside the claustrum, whereas 21.0% and 14.3% of PV-shell neuronal dendrites and axons, respectively, and 25.0% and 35.2% of SOM-shell neuronal dendrites and axons, respectively, were distributed outside the claustrum. The dendrites and axons of PV-shell neurons outside the claustrum were observed in the areas adjacent to the claustrum such as the insular cortex (dendrites, PV-shell #4, 6, 7; axons, #4, 5, 6, 7; Fig. $6C_2$ and Fig. S4) and dorsal endopiriform nucleus (DEn; dendrites,

PV-shell #5, 7; axons, #4, 5, 6, 7; Fig. 6C_2 and Fig. S4). The dendrites or axons of SOM-shell neurons were also found in the insular cortex (dendrites, SOM-shell #12, 13, 15; axons, #11, 12, 13, 14, 15; Fig. 6D_2 and Fig. S4) and DEn (dendrites, SOM-shell #11, 12, 15; axons, #11, 12, 14, 15; Fig. 6D_2 and Fig. S4). Additionally, a few axon collaterals of a SOM-shell neuron were detected in somatosensory and motor cortical areas (SOM-shell #15; Fig. S4). Considering that almost all SOM neurons showed the signals for GAD67 mRNA and that a population of GABAergic projection neurons is known to be positive for SOM in the cerebral cortices (Tomioka et al., 2005), this SOM-shell neuron may correspond to a long-range projecting inhibitory neuron previously reported in the claustrum (Shelton et al., 2022).

Directional preferences in the dendritic and axonal arborizations of PV and SOM neurons in the core and ventral shell regions

We then quantified the ramifications of three-dimensionally reconstructed dendrites and axons of PV and SOM neurons in the core and ventral shell regions by counting the number of intersections between neuronal processes and concentric spheres centered at the soma (3D Sholl analysis) (Sholl, 1953). Subsequent statistical multiple comparisons were conducted for dendrites or axons among PV-core, PV-shell, SOM-core, and SOM-shell neurons (Fig. 7). The number of dendritic ramifications was not significantly different between PV-core and PV-shell neurons and between SOM-core and SOM-shell neurons. We found that the dendrites of PV-core neurons were more highly ramified than those of SOM-core neurons at 50–250 μm. We also observed that PV-shell neurons had more extensively ramified dendrites than SOM-shell neurons at 50–300 μm (Fig. 7A). These results indicate that the dendritic arborizations of PV and SOM neurons are not different between the core and ventral shell regions and that PV neurons have more abundant dendritic branching than SOM neurons.

In 3D Sholl analysis for axons, we found that all four types of neurons had prominent axonal arborizations around 200 μm from the soma and that those axons were widely distributed up to more than 800 μm. The axonal ramifications were similar in PV-core, SOM-core, and PV-shell neurons, whereas those in SOM-shell neurons were sparser at 150–200 μm and more abundant at 400–700 μm (Fig. 7B), suggesting that SOM-shell neurons tend to innervate more distal portions than the other types of neurons.

It was recently reported that intraclaustral connections mediated by glutamatergic neurons are predominant along the RC axis (Orman, 2015; Shelton et al., 2022). To examine whether PV and SOM neurons have such a directional preference, we projected three-dimensionally reconstructed neurons onto a plane along three orthogonal RC, ML, or DV axes (ML–DV, DV–RC, or RC–ML plane), and quantified the ramifications of dendrites and axons on these three planes (2D Sholl analysis; Fig. 8). The dendritic branching of PV-core and SOM-core

neurons were almost similar among the three ML–DV, DV–RC, and RC–ML planes, but the branching in the ML–DV plane was low in the distal portion compared with that in the other planes (Fig. 8A, B, left). The dendrites of PV-shell and SOM-shell neurons also showed similar branching patterns, although their dendrites extending more than 150 μm from the soma were less branched on the RC–ML plane than on the ML–DV and DV–RC planes (Fig. 8C, D, left). These results indicate that PV and SOM neurons distribute the dendrites almost uniformly in the core and ventral shell regions.

In contrast to dendrites, the axonal arborizations on the ML–DV plane were distinct from those in the RC–ML and DV–RC planes. The axons of PV-core and SOM-core neurons on the ML–DV plane were confined to less than 400 μm, whereas those on the DV–RC and RC–ML planes widely extended over 700 μm (Fig. 8A, B, right). The axons of PV-shell neurons on the ML–DV plane were observed mostly within 500 μm and those on the DV–RC and RC–ML planes spread over 700 μm. The axons of SOM-shell neurons were broadly distributed over 800 μm on all three planes, but those on the ML–DV plane were significantly lower than those on the DV–RC and RC–ML planes over 300 μm from the soma. (Fig. 8C, D, right). These findings indicate that PV and SOM neurons in the core and ventral shell regions preferentially spread their axons along the RC axis to distal portions.

Discussion

In the present study, we showed that GABAergic neurons accounted for approximately 10% of claustral neurons and that PV, SOM, and VIP neurons constituted approximately 20%, 30%, and 10% of claustral GABAergic neurons, respectively. Furthermore, we demonstrated that PV-core and SOM-core neurons confined their dendrites and axons within the subregion, while PV-shell and SOM-shell neurons avoided extending their neurites into the core region.

We divided the mouse claustrum into the core and shell regions based on cytoarchitecture (Fig. 1), referring to the previous studies (Atlan et al., 2017; Binks et al., 2019; Marriott et al., 2021; Ham and Augustine, 2022; Shelton et al., 2022). However, whether the shell region is included in the claustrum remains debatable in rodents. Several studies have argued that the claustrum contains only the core region and that the shell regions belong to the insular cortex (Mathur, 2014; Wang et al., 2017; Dillingham et al., 2019; Grimstvedt et al., 2022; Wang et al., 2022). On the other hand, ISH histochemical and single-cell RNA sequencing (scRNA-seq) analyses demonstrated that the two regions displayed shared gene expressions such as *Gnb4*, *Nr4a2*, *Synpr*, and *Gng2* (Watakabe, 2017; Watson and Puelles, 2017; Smith et al., 2019), which distinguish the claustrum from the insular cortex (Binks et al., 2019; Smith et al., 2019; Erwin et al., 2021). Moreover, reciprocal connections with cortical areas are observed in both the core and shell regions (Atlan et al., 2017; Marriott et al., 2021; Ham and Augustine, 2022). We thus considered the shell regions to be a part of the claustrum in the present study.

We demonstrated that 9–11% of claustral neurons expressed GAD67 mRNA, and GABAergic neurons appeared to be uniformly distributed among the claustral subregions (Table 1; Fig. 2). This proportion of GABAergic neurons found in our study is in concordance with those of previous reports of rabbits and humans: 12% of claustral neurons in rabbits displayed immunoreactivity for GABA in the claustrum (Gomez-Urquijo et al., 2000), and 7% of claustral neurons in humans comprised aspiny interneurons and homogeneously distributed throughout the claustrum (Braak and Braak, 1982; Spahn and Braak, 1985). We also found that 88–90% of claustral neurons expressed VGluT1 mRNA. This finding is consistent with the results of a single-molecule FISH study, where VGluT1 and GAD65 mRNAs were expressed in 83% and 4% of DAPI-positive cells in the mouse claustrum, respectively (Atlan et al., 2018). The slight differences in population rates between the present and previous studies might be explained by the differences in total cells counted. In the present study we counted NeuN-immunoreactive cells as total cells, whereas the previous study counted DAPI-positive cells, which were assumed to include both neuronal and glial cells. Although the single-molecule FISH study also reported that a population of GAD65-expressing neurons showed the signals for VGluT1 mRNA as well (Atlan et al., 2018), we found that the signals for VGluT1 and GAD67 mRNAs did not colocalize (Fig. S2). The discrepancy between the present and previous studies could be due to the mRNA each

study targeted (*GAD67* or *GAD65*). It was also reported that part of claustral neurons expressed VGluT2 or VGluT3 mRNA and that VGluT2-expressing neurons had projections to the cortex (Hur and Zaborszky, 2005; Johnson et al., 2014; Hawrylycz et al., 2015; Xu et al., 2022), suggesting the diversity of glutamatergic neurons as well as of GABAergic neurons.

Our immunohistochemical analysis clarified that PV, SOM, and VIP neurons occupied 20%, 30%, and 10% of claustral GABAergic neurons, respectively (Table 2; Fig. 3), and had little overlap with each other (Table 3; Fig. 4). An electrophysiological study demonstrated that PV, SOM, and VIP neurons in the mouse claustrum could be distinguished by their intrinsic electrical properties (Graf et al., 2020). These immunohistological and electrophysiological findings indicate that PV, SOM, and VIP neurons form distinct subgroups. The three types of neurons covered approximately 60% of claustral GABAergic neurons, but the residual population remained undetermined in the present study. It has been shown that the claustrum contains various GABAergic neurons immunoreactive for neurochemical markers, such as calbindin, calretinin, cholecystokinin, neuropeptide Y (NPY), and nitric oxide synthase (Eiden et al., 1990; Druga et al., 1993; Kowianski et al., 2001; Guirado et al., 2003; Real et al., 2003; Davila et al., 2005; Kowianski et al., 2008; Druga et al., 2014; Marriott et al., 2021). Among them, NPY-positive neurons were reported to comprise a 1.5-fold larger population than SOM neurons in the mouse claustrum and to show considerable overlap with SOM immunoreactivity; 50% of SOM neurons displayed immunoreactivity for NPY, and conversely, 33% of NPY neurons were positive for SOM (Marriott et al., 2021). To clarify the heterogeneity of residual neurons in detail, it would be useful to thoroughly examine the gene expression patterns of claustral GABAergic neurons. Indeed, recent technical advances in scRNA-seq have revealed the transcriptional signatures of glutamatergic neurons in the core and ventral shell regions in mice (Erwin et al., 2021) and the homologue of claustrum in reptiles (Norimoto et al., 2020). Integration of transcriptomic, morphological, and electrophysiological analyses would provide clearer insights for the diversity of claustral GABAergic neurons.

The topographic organization of reciprocal connections between the claustrum and cerebral cortex is uniformly elongated across the RC axis in the claustrum (Atlan et al., 2017; Marriott et al., 2021; Ham and Augustine, 2022). Notably, the intrinsic connectivity of claustral glutamatergic neurons also shows similar RC continuity (Smith and Alloway, 2010; Jackson et al., 2020); the axons of claustral projecting neurons traveled along the RC axis inside the claustrum (Wang et al., 2022), and the intraclaustral connections mediated by glutamatergic synapses were prominently observed in this direction (Orman, 2015; Shelton et al., 2022). In the present study, we demonstrated that PV and SOM neurons in the core and ventral shell regions preferentially extended their axons more than 800 μm along the RC direction (Fig. 8). Taken

together, the claustrum is suggested to be tightly bounded in the RC direction via both glutamatergic and GABAergic neurons.

In contrast to the RC axis, the topographical arrangement of claustrocortical neurons is found across the DV and/or ML directions (Atlan et al., 2017; Marriott et al., 2021; Ham and Augustine, 2022). Further, the claustral glutamatergic neurons form few axon collaterals inside the claustrum (Wang et al., 2022) and rarely make their intraclaustral connections in the DV and/or ML directions (Orman, 2015; Kim et al., 2016). We here demonstrated that the dendrites and axons of PV and SOM neurons in the core and shell regions were mostly confined within each subregion, but that the neurites were widely developed within each subregion (Fig. 6; Table 4). PV-core and SOM-core neurons extended the dendrites partially to the shell region (23% in PV-core neurons; 16% in SOM-core neurons; Table 4). Because the topographical arrangement between the claustrum and cerebral cortex is reported to overlap in part across the core and shell regions (Marriott et al., 2021; Shelton et al., 2022), the intersections of the dendrites of PV-core and SOM-core neurons with the shell region might reflect the gradual transitions of the topography within the claustrum. Furthermore, 3D and 2D Sholl analyses revealed that these neurons extended their dendrites almost uniformly, and that the axons densely spread along not only the RC axis but also DV and ML axes. Previous electron microscopic and electrophysiological studies have shown that claustral GABAergic neurons receive synaptic inputs from corticoclaustral, claustrocortical, and GABAergic neurons (LeVay and Sherk, 1981; Kim et al., 2016; Day-Brown et al., 2017; White et al., 2018). It is therefore suggested that claustral PV and SOM neurons integrate multiple neuronal information within the core and shell regions but not between those two subregions.

As indicated by a previous report (Marriott et al., 2021), we observed that neuronal fibers immunoreactive for PV were densely distributed in the core region, whereas those for SOM were in the shell region (Fig. 4). As the cell bodies of PV and SOM neurons were uniformly distributed in the core and shell regions, respectively, we hypothesized that the neurite extensions of PV and SOM neurons might be localized within the core and shell regions, respectively. After 3D reconstructions of PV and SOM neurons, we noticed that neither of the neurons showed substantial differences in the spread of neurites between the core and shell regions. Thus, the particular distribution of immunoreactivities for PV and SOM in the core and shell regions might be explained by other factors. One possibility is that the claustral subregions receive the axons containing these proteins from the outside areas of the claustrum. A population of neocortical pyramidal neurons in layer V and thalamic relay neurons are known to express PV protein (Tanahira et al., 2009). It is also reported that some SOM neurons send long-range projections in the cortical and subcortical areas (Tomioka et al., 2015; Eyre and Bartos, 2019; Xiao et al., 2021). It could be possible that the extrinsic axonal fibers containing PV protein and SOM peptide

innervate the core and shell regions, respectively, and contribute to the differential immunoreactivities within the claustral subregions. There is another possibility that claustral GABAergic neurons in the core and shell subregions show differential expression levels of PV protein and SOM peptide. Our neuronal labeling experiments with virus vectors demonstrated the neuronal fibers of PV neurons in the shell region and those of SOM neurons in the core region (Fig. 6). Immunofluorescence labeling also detected the neuronal fibers immunoreactive for PV in the shell region, although these immunoreactivities were weaker than in the core region, and vice versa for SOM (Marriott et al., 2021; Fig. 4). Therefore, the amount and/or localization of PV protein and SOM peptide might be different between the GABAergic neurons in the core and shell regions. The expression level of PV protein is reported to be affected by synaptic activities (Patz et al., 2004; Donato et al., 2013). SOM peptide work as a neurotransmitter and is involved in synaptic plasticity through its receptors (Liguz-Lecznar et al., 2016). Comparison of the expression levels of PV protein and SOM peptide between the core and shell regions with scRNA-seq and/or reverse transcription quantitative PCR would be beneficial for further understanding the role of these neurons in the claustral core and shell organization.

Conclusions

The present study showed that claustral GABAergic neurons are homogeneously distributed and that PV and SOM neurons are compartmentalized in the claustral subregions. Claustral PV and SOM neurons might participate in independent information processing within the local circuits of the core and shell regions.

Glossary

2D: two dimensional

3D: three dimensional

AAV: adeno-associated virus

AF: Alexa Fluor

AI: agranular insular cortex

APS: 3-aminopropyltriethoxysilane

BGHpA: polyadenylation signal derived from the bovine growth hormone gene

BSA: bovine serum albumin

BT: biotinylated tyramine

CMV: cytomegalovirus

DAPI: 4',6-Diamidino-2-phenylindole

DEn: dorsal endopiriform nucleus

DI: dysgranular insular cortex

DIG: digoxigenin

DV: dorsoventral

FISH: fluorescence in situ hybridization

FITC: fluorescein

FLEX: flip-excision

FT: fluorochromized tyramide

GAD67: glutamic acid decarboxylase 67 kDa isoform

GO: glucose oxidase

ML: mediolateral

NeuN: neuronal nuclei

NPY: neuropeptide Y

palGFP: EGFP with a palmitoylation signal derived from the GAP-43 N-terminus

PV: parvalbumin

RC: rostrocaudal

scRNA-seq: single-cell RNA sequencing

SDCM: spinning disk confocal microscope

SOM: somatostatin

TRE_{tight}: Tet-responsive promoter with modified Tet response element

tTAad: improved version of a tetracycline-controlled transactivator

VGluT1: vesicular glutamate transporter 1

VIP: vasoactive intestinal polypeptide

WPRE: woodchuck hepatitis virus posttranscriptional regulatory element

Author contributions

Conceptualization, M.T., T.I., and H.H.; Methodology, M.T., K.Y., S.O., K.O., and H.H.; Investigation, M.T., T.K., H.M., and H.H.; Resources, Y.I. and M.W.; Writing – Original Draft, M.T. and H.H.; Writing – Review & Editing, M.T., T.K., H.M., K.Y., S.O., K.O., Y.I., M.K., M.W., T.I., and H.H.; Project Administration, H.H; Funding Acquisition, M.T., K.Y., K.O., M.K., M.W., T.I., and H.H. All authors have approved the final article.

Declarations of interest:

None.

Acknowledgments

We thank Ayaka Ansai and Naoko Imai (Juntendo University) for technical help. We would also like to thank Editage (www.editage.com) for English language editing. This study was supported in part by KAKENHI (JP22J15034 to M.T.; JP20K07231 to K.Y.; JP19J01590 and JP20K16112 to K.O.; JP20K07743 to M.K.; JP21H02589 and JP20H05628 to M.W.; JP21H02592 to H.H.) from the Japan Society for the Promotion of Science (JSPS). This study was also supported by the Japan Agency for Medical Research and Development (AMED; JP19dm0207093 and JP18dm0207020 to T.I.; JP21dm0207112 to H.H.), Moonshot R&D from the Japan Science and Technology Agency (JST; JPMJMS2024 to H.H.), Fusion Oriented Research for disruptive Science and Technology (FOREST) from JST (JPMJFR204D to H.H.).

References

Atlan, G., Matosevich, N., Peretz-Rivlin, N., Yvgi, I., Chen, E., Kleinman, T., Bleistein, N., Sheinbach, E., Groysman, M., Nir, Y., Citri, A., 2021. Claustral Projections to Anterior Cingulate Cortex Modulate Engagement with the External World. bioRxiv, 2021.2006.2017.448649.

Atlan, G., Terem, A., Peretz-Rivlin, N., Groysman, M., Citri, A., 2017. Mapping synaptic cortico-claustral connectivity in the mouse. J Comp Neurol 525, 1381-1402.

Atlan, G., Terem, A., Peretz-Rivlin, N., Sehrawat, K., Gonzales, B.J., Pozner, G., Tasaka, G.I., Goll, Y., Refaeli, R., Zviran, O., Lim, B.K., Groysman, M., Goshen, I., Mizrahi, A., Nelken, I., Citri, A., 2018. The Claustrum Supports Resilience to Distraction. Curr Biol 28, 2752-2762 e2757.

Binks, D., Watson, C., Puelles, L., 2019. A Re-evaluation of the Anatomy of the Claustrum in Rodents and Primates-Analyzing the Effect of Pallial Expansion. Front Neuroanat 13, 34.

Braak, H., Braak, E., 1982. Neuronal types in the claustrum of man. Anat Embryol (Berl) 163, 447-460.

Chevee, M., Finkel, E.A., Kim, S.J., O'Connor, D.H., Brown, S.P., 2022. Neural activity in the mouse claustrum in a cross-modal sensory selection task. Neuron 110, 486-501 e487.

Chia, Z., Augustine, G.J., Silberberg, G., 2020. Synaptic Connectivity between the Cortex and Claustrum Is Organized into Functional Modules. Curr Biol 30, 2777-2790 e2774.

Crick, F.C., Koch, C., 2005. What is the function of the claustrum? Philos Trans R Soc Lond B Biol Sci 360, 1271-1279.

Davila, J.C., Real, M.A., Olmos, L., Legaz, I., Medina, L., Guirado, S., 2005. Embryonic and postnatal development of GABA, calbindin, calretinin, and parvalbumin in the mouse claustral complex. J Comp Neurol 481, 42-57.

Day-Brown, J.D., Slusarczyk, A.S., Zhou, N., Quiggins, R., Petry, H.M., Bickford, M.E., 2017. Synaptic organization of striate cortex projections in the tree shrew: A comparison of the claustrum and dorsal thalamus. J Comp Neurol 525, 1403-1420.

Dillingham, C.M., Mathiasen, M.L., Frost, B.E., Lambert, M.A.C., Bubb, E.J., Jankowski, M.M., Aggleton, J.P., O'Mara, S.M., 2019. The Anatomical Boundary of the Rat Claustrum. Front Neuroanat 13, 53.

Donato, F., Rompani, S.B., Caroni, P., 2013. Parvalbumin-expressing basket-cell network plasticity induced by experience regulates adult learning. Nature 504, 272-276.

Druga, R., Chen, S., Bentivoglio, M., 1993. Parvalbumin and calbindin in the rat claustrum: an immunocytochemical study combined with retrograde tracing frontoparietal cortex. J Chem Neuroanat 6, 399-406.

Druga, R., Salaj, M., Barinka, F., Edelstein, L., Kubova, H., 2014. Calretinin immunoreactivity in the claustrum of the rat. Front Neuroanat 8, 160.

Eiden, L.E., Mezey, E., Eskay, R.L., Beinfeld, M.C., Palkovits, M., 1990. Neuropeptide content and connectivity of the rat claustrum. Brain Res 523, 245-250.

Erwin, S.R., Bristow, B.N., Sullivan, K.E., Kendrick, R.M., Marriott, B., Wang, L., Clements, J., Lemire, A.L., Jackson, J., Cembrowski, M.S., 2021. Spatially patterned excitatory neuron subtypes and projections of the claustrum. Elife 10.

Eyre, M.D., Bartos, M., 2019. Somatostatin-Expressing Interneurons Form Axonal Projections to the Contralateral Hippocampus. Front Neural Circuits 13, 56.

Ferreira, T.A., Blackman, A.V., Oyrer, J., Jayabal, S., Chung, A.J., Watt, A.J., Sjostrom, P.J., van Meyel, D.J., 2014. Neuronal morphometry directly from bitmap images. Nat Methods 11, 982-984.

Furuta, T., Kaneko, T., Deschenes, M., 2009. Septal neurons in barrel cortex derive their receptive field input from the lemniscal pathway. J Neurosci 29, 4089-4095.

Furuta, T., Tomioka, R., Taki, K., Nakamura, K., Tamamaki, N., Kaneko, T., 2001. In vivo transduction of central neurons using recombinant Sindbis virus: Golgi-like labeling of dendrites and axons with membrane-targeted fluorescent proteins. J Histochem Cytochem 49, 1497-1508.

Furuta, T., Yamauchi, K., Okamoto, S., Takahashi, M., Kakuta, S., Ishida, Y., Takenaka, A., Yoshida, A., Uchiyama, Y., Koike, M., Isa, K., Isa, T., Hioki, H., 2022. Multi-scale light microscopy/electron microscopy neuronal imaging from brain to synapse with a tissue clearing method, Sca*l*eSF. iScience 25, 103601.

Goll, Y., Atlan, G., Citri, A., 2015. Attention: the claustrum. Trends Neurosci 38, 486-495.

Gomez-Urquijo, S.M., Gutierrez-Ibarluzea, I., Bueno-Lopez, J.L., Reblet, C., 2000. Percentage incidence of gamma-aminobutyric acid neurons in the claustrum of the rabbit and comparison with the cortex and putamen. Neurosci Lett 282, 177-180.

Graf, M., Nair, A., Wong, K.L.L., Tang, Y., Augustine, G.J., 2020. Identification of Mouse Claustral Neuron Types Based on Their Intrinsic Electrical Properties. eNeuro 7.

Grimstvedt, J.S., Shelton, A.M., Hoerder-Suabedissen, A., Oliver, D.K., Berndtsson, C.H., Blankvoort, S., Nair, R.R., Packer, A.M., Witter, M.P., Kentros, C.G., 2022. A multifaceted architectural framework of the mouse claustrum complex. bioRxiv, 2022.2006.2002.494429.

Guirado, S., Real, M.A., Olmos, J.L., Davila, J.C., 2003. Distinct types of nitric oxide-producing neurons in the developing and adult mouse claustrum. J Comp Neurol 465, 431-444.

Ham, G.X., Augustine, G.J., 2022. Topologically Organized Networks in the Claustrum Reflect Functional Modularization. Front Neuroanat 16, 901807.

Hama, H., Hioki, H., Namiki, K., Hoshida, T., Kurokawa, H., Ishidate, F., Kaneko, T., Akagi, T., Saito, T., Saido, T., Miyawaki, A., 2015. Sca*l*eS: an optical clearing palette for biological imaging. Nat Neurosci 18, 1518-1529.

Harris, C.R., Millman, K.J., van der Walt, S.J., Gommers, R., Virtanen, P., Cournapeau, D., Wieser, E., Taylor, J., Berg, S., Smith, N.J., Kern, R., Picus, M., Hoyer, S., van Kerkwijk, M.H., Brett, M., Haldane, A., Del Rio, J.F., Wiebe, M., Peterson, P., Gerard-Marchant, P., Sheppard, K., Reddy, T., Weckesser, W., Abbasi, H., Gohlke, C., Oliphant, T.E., 2020. Array programming with NumPy. Nature 585, 357-362.

Hawrylycz, M., Miller, J.A., Menon, V., Feng, D., Dolbeare, T., Guillozet-Bongaarts, A.L., Jegga, A.G., Aronow, B.J., Lee, C.K., Bernard, A., Glasser, M.F., Dierker, D.L., Menche, J., Szafer, A., Collman, F., Grange, P., Berman, K.A., Mihalas, S., Yao, Z., Stewart, L., Barabasi, A.L., Schulkin, J., Phillips, J., Ng, L., Dang, C., Haynor, D.R., Jones, A., Van Essen, D.C., Koch, C., Lein, E., 2015. Canonical genetic signatures of the adult human brain. Nat Neurosci 18, 1832-1844.

Hioki, H., Kuramoto, E., Konno, M., Kameda, H., Takahashi, Y., Nakano, T., Nakamura, K.C., Kaneko, T., 2009. High-level transgene expression in neurons by lentivirus with Tet-Off system. Neurosci Res 63, 149-154.

Hioki, H., Nakamura, H., Ma, Y.F., Konno, M., Hayakawa, T., Nakamura, K.C., Fujiyama, F., Kaneko, T., 2010. Vesicular glutamate transporter 3-expressing nonserotonergic projection neurons constitute a subregion in the rat midbrain raphe nuclei. J Comp Neurol 518, 668-686.

Hioki, H., Sohn, J., Nakamura, H., Okamoto, S., Hwang, J., Ishida, Y., Takahashi, M., Kameda, H., 2018. Preferential inputs from cholecystokinin-positive neurons to the somatic compartment of parvalbumin-expressing neurons in the mouse primary somatosensory cortex. Brain Res 1695, 18-30.

Hippenmeyer, S., Vrieseling, E., Sigrist, M., Portmann, T., Laengle, C., Ladle, D.R., Arber, S., 2005. A developmental switch in the response of DRG neurons to ETS transcription factor signaling. PLoS Biol 3, e159.

Hunter, J.D., 2007. Matplotlib: A 2D Graphics Environment. Comput Sci Eng 9, 90-95.

Hur, E.E., Zaborszky, L., 2005. Vglut2 afferents to the medial prefrontal and primary somatosensory cortices: a combined retrograde tracing in situ hybridization study [corrected]. J Comp Neurol 483, 351-373.

Jackson, J., Smith, J.B., Lee, A.K., 2020. The Anatomy and Physiology of Claustrum-Cortex Interactions. Annu Rev Neurosci 43, 231-247.

Johnson, J.I., Fenske, B.A., Jaswa, A.S., Morris, J.A., 2014. Exploitation of puddles for breakthroughs in claustrum research. Front Syst Neurosci 8, 78.

Kim, J., Matney, C.J., Roth, R.H., Brown, S.P., 2016. Synaptic Organization of the Neuronal Circuits of the Claustrum. J Neurosci 36, 773-784.

Kitanishi, T., Matsuo, N., 2017. Organization of the Claustrum-to-Entorhinal Cortical Connection in Mice. J Neurosci 37, 269-280.

Kowianski, P., Morys, J.M., Dziewiatkowski, J., Wojcik, S., Sidor-Kaczmarek, J., Morys, J., 2008. NPY-, SOM- and VIP-containing interneurons in postnatal development of the rat claustrum. Brain Res Bull 76, 565-571.

Kowianski, P., Timmermans, J.P., Morys, J., 2001. Differentiation in the immunocytochemical features of intrinsic and cortically projecting neurons in the rat claustrum -- combined immunocytochemical and axonal transport study. Brain Res 905, 63-71.

Kuramoto, E., Furuta, T., Nakamura, K.C., Unzai, T., Hioki, H., Kaneko, T., 2009. Two types of thalamocortical projections from the motor thalamic nuclei of the rat: a single neuron-tracing study using viral vectors. Cereb Cortex 19, 2065-2077.

LeVay, S., Sherk, H., 1981. The visual claustrum of the cat. I. Structure and connections. J Neurosci 1, 956-980.

Liguz-Lecznar, M., Urban-Ciecko, J., Kossut, M., 2016. Somatostatin and Somatostatin-Containing Neurons in Shaping Neuronal Activity and Plasticity. Front Neural Circuits 10, 48.

Linkert, M., Rueden, C.T., Allan, C., Burel, J.M., Moore, W., Patterson, A., Loranger, B., Moore, J., Neves, C., Macdonald, D., Tarkowska, A., Sticco, C., Hill, E., Rossner, M., Eliceiri, K.W., Swedlow, J.R., 2010. Metadata matters: access to image data in the real world. J Cell Biol 189, 777-782.

Liu, J., Wu, R., Johnson, B., Vu, J., Bass, C., Li, J.X., 2019. The Claustrum-Prefrontal Cortex Pathway Regulates Impulsive-Like Behavior. J Neurosci 39, 10071-10080.

Ma, Y., Hioki, H., Konno, M., Pan, S., Nakamura, H., Nakamura, K.C., Furuta, T., Li, J.L., Kaneko, T., 2011. Expression of gap junction protein connexin36 in multiple subtypes of GABAergic neurons in adult rat somatosensory cortex. Cereb Cortex 21, 2639-2649.

Marriott, B.A., Do, A.D., Zahacy, R., Jackson, J., 2021. Topographic gradients define the projection patterns of the claustrum core and shell in mice. J Comp Neurol 529, 1607-1627.

Mathur, B.N., 2014. The claustrum in review. Front Syst Neurosci 8, 48.

McKinney, W., Van Der Walt, S., Millman, J., 2010. Proceedings of the 9th Python in Science Conference. Austin, Texas.

Miyawaki, A., Hama, H., Hioki, H., Namiki, K., Hoshida, T., Kurokawa, H., 2016. Deep Imaging of Cleared Brain by Confocal Laser-Scanning Microscopy. Protocol exchange.

Moriyoshi, K., Richards, L.J., Akazawa, C., O'Leary, D.D., Nakanishi, S., 1996. Labeling neural cells using adenoviral gene transfer of membrane-targeted GFP. Neuron 16, 255-260.

Nakamura, K., Watakabe, A., Hioki, H., Fujiyama, F., Tanaka, Y., Yamamori, T., Kaneko, T., 2007. Transiently increased colocalization of vesicular glutamate transporters 1 and 2 at single axon terminals during postnatal development of mouse neocortex: a quantitative analysis with correlation coefficient. Eur J Neurosci 26, 3054-3067.

Narikiyo, K., Mizuguchi, R., Ajima, A., Shiozaki, M., Hamanaka, H., Johansen, J.P., Mori, K., Yoshihara, Y., 2020. The claustrum coordinates cortical slow-wave activity. Nat Neurosci 23, 741-753.

Norimoto, H., Fenk, L.A., Li, H.H., Tosches, M.A., Gallego-Flores, T., Hain, D., Reiter, S., Kobayashi, R., Macias, A., Arends, A., Klinkmann, M., Laurent, G., 2020. A claustrum in reptiles and its role in slow-wave sleep. Nature 578, 413-418.

Obst-Pernberg, K., Medina, L., Redies, C., 2001. Expression of R-cadherin and N-cadherin by cell groups and fiber tracts in the developing mouse forebrain: relation to the formation of functional circuits. Neuroscience 106, 505-533.

Okamoto, S., Sohn, J., Tanaka, T., Takahashi, M., Ishida, Y., Yamauchi, K., Koike, M., Fujiyama, F., Hioki, H., 2020. Overlapping Projections of Neighboring Direct and Indirect Pathway Neostriatal Neurons to Globus Pallidus External Segment. iScience, 101409.

Okamoto, S., Yamauchi, K., Sohn, J., Takahashi, M., Ishida, Y., Furuta, T., Koike, M., Fujiyama, F., Hioki, H., 2021. Exclusive labeling of direct and indirect pathway neurons in the mouse neostriatum by an adeno-associated virus vector with Cre/lox system. STAR Protoc 2, 100230.

Orman, R., 2015. Claustrum: a case for directional, excitatory, intrinsic connectivity in the rat. J Physiol Sci 65, 533-544.

Patz, S., Grabert, J., Gorba, T., Wirth, M.J., Wahle, P., 2004. Parvalbumin expression in visual cortical interneurons depends on neuronal activity and TrkB ligands during an Early period of postnatal development. Cereb Cortex 14, 342-351.

Paxinos, G., Franklin., K.B.J., 2007. The Mouse Brain in Stereotaxic Coordinates. Elsevier Science.

Real, M.A., Davila, J.C., Guirado, S., 2003. Expression of calcium-binding proteins in the mouse claustrum. J Chem Neuroanat 25, 151-160.

Real, M.A., Davila, J.C., Guirado, S., 2006. Immunohistochemical localization of the vesicular glutamate transporter VGLUT2 in the developing and adult mouse claustrum. J Chem Neuroanat 31, 169-177.

Schindelin, J., Arganda-Carreras, I., Frise, E., Kaynig, V., Longair, M., Pietzsch, T., Preibisch, S., Rueden, C., Saalfeld, S., Schmid, B., Tinevez, J.Y., White, D.J., Hartenstein, V., Eliceiri, K., Tomancak, P., Cardona, A., 2012. Fiji: an open-source platform for biological-image analysis. Nat Methods 9, 676-682.

Schnutgen, F., Doerflinger, N., Calleja, C., Wendling, O., Chambon, P., Ghyselinck, N.B., 2003. A directional strategy for monitoring Cre-mediated recombination at the cellular level in the mouse. Nat Biotechnol 21, 562-565.

Shelton, A.M., Oliver, D.K., Grimstvedt, J.S., Lazarte, I.P., Kapoor, I., Swann, J.A., Ashcroft, C.A., Williams, S.N., Conway, N., Robinson, A., Kentros, C.G., Witter, M.P., Butt, S.J.B., Packer, A.M., 2022. Single neurons and networks in the claustrum integrate input from widespread cortical sources. bioRxiv, 2022.2005.2006.490864.

Sholl, D.A., 1953. Dendritic organization in the neurons of the visual and motor cortices of the cat. J Anat 87, 387-406.

Smith, J.B., Alloway, K.D., 2010. Functional specificity of claustrum connections in the rat: interhemispheric communication between specific parts of motor cortex. J Neurosci 30, 16832-16844.

Smith, J.B., Alloway, K.D., Hof, P.R., Orman, R., Reser, D.H., Watakabe, A., Watson, G.D.R., 2019. The relationship between the claustrum and endopiriform nucleus: A perspective towards consensus on cross-species homology. J Comp Neurol 527, 476-499.

Smith, J.B., Lee, A.K., Jackson, J., 2020. The claustrum. Curr Biol 30, R1401-R1406.

Smythies, J., Edelstein, L., Ramachandran, V., 2012. Hypotheses relating to the function of the claustrum. Front Integr Neurosci 6, 53.

Sohn, J., Hioki, H., Okamoto, S., Kaneko, T., 2014. Preprodynorphin-expressing neurons constitute a large subgroup of somatostatin-expressing GABAergic interneurons in the mouse neocortex. J Comp Neurol 522, 1506-1526.

Sohn, J., Takahashi, M., Okamoto, S., Ishida, Y., Furuta, T., Hioki, H., 2017. A Single Vector Platform for High-Level Gene Transduction of Central Neurons: Adeno-Associated Virus Vector Equipped with the Tet-Off System. PLoS One 12, e0169611.

Spahn, B., Braak, H., 1985. Percentage of projection neurons and various types of interneurons in the human claustrum. Acta Anat (Basel) 122, 245-248.

Takahashi, M., Ishida, Y., Kataoka, N., Nakamura, K., Hioki, H., 2021. Efficient Labeling of Neurons and Identification of Postsynaptic Sites Using Adeno-Associated Virus Vector, In: Lujan, R., Ciruela, F. (Eds.), Receptor and Ion Channel Detection in the Brain. Springer US, New York, NY, pp. 323-341.

Tamamaki, N., Nakamura, K., Furuta, T., Asamoto, K., Kaneko, T., 2000. Neurons in Golgi-stain-like images revealed by GFP-adenovirus infection in vivo. Neurosci Res 38, 231-236.

Tamamaki, N., Yanagawa, Y., Tomioka, R., Miyazaki, J., Obata, K., Kaneko, T., 2003. Green fluorescent protein expression and colocalization with calretinin, parvalbumin, and somatostatin in the GAD67-GFP knock-in mouse. J Comp Neurol 467, 60-79.

Tanahira, C., Higo, S., Watanabe, K., Tomioka, R., Ebihara, S., Kaneko, T., Tamamaki, N., 2009. Parvalbumin neurons in the forebrain as revealed by parvalbumin-Cre transgenic mice. Neurosci Res 63, 213-223.

Taniguchi, H., He, M., Wu, P., Kim, S., Paik, R., Sugino, K., Kvitsiani, D., Fu, Y., Lu, J., Lin, Y., Miyoshi, G., Shima, Y., Fishell, G., Nelson, S.B., Huang, Z.J., 2011. A resource of Cre driver lines for genetic targeting of GABAergic neurons in cerebral cortex. Neuron 71, 995-1013.

Terem, A., Gonzales, B.J., Peretz-Rivlin, N., Ashwal-Fluss, R., Bleistein, N., Del Mar Reus-Garcia, M., Mukherjee, D., Groysman, M., Citri, A., 2020. Claustral Neurons Projecting to Frontal Cortex Mediate Contextual Association of Reward. Curr Biol 30, 3522-3532 e3526.

Tomioka, R., Okamoto, K., Furuta, T., Fujiyama, F., Iwasato, T., Yanagawa, Y., Obata, K., Kaneko, T., Tamamaki, N., 2005. Demonstration of long-range GABAergic connections distributed throughout the mouse neocortex. Eur J Neurosci 21, 1587-1600.

Tomioka, R., Sakimura, K., Yanagawa, Y., 2015. Corticofugal GABAergic projection neurons in the mouse frontal cortex. Front Neuroanat 9, 133.

Wang, Q., Ng, L., Harris, J.A., Feng, D., Li, Y., Royall, J.J., Oh, S.W., Bernard, A., Sunkin, S.M., Koch, C., Zeng, H., 2017. Organization of the connections between claustrum and cortex in the mouse. J Comp Neurol 525, 1317-1346.

Wang, Q., Wang, Y., Xie, P., Kuo, H.-C., Hirokawa, K.E., Naeemi, M., Yao, S., Ouellette, B., Mallory, M., Lesnar, P., Kuang, X., Li, Y., Ye, M., Chen, C., Xiong, W., Ahmadinia, L., El-Hifnawi, L., Cetin, A., Harris, J.A., Zeng, H., Koch, C., 2022. Regional and cell type-specific afferent and efferent projections of the mouse claustrum. bioRxiv, 2022.2002.2023.481555.

Watakabe, A., 2017. In situ hybridization analyses of claustrum-enriched genes in marmosets. J Comp Neurol 525, 1442-1458.

Watson, C., Puelles, L., 2017. Developmental gene expression in the mouse clarifies the organization of the claustrum and related endopiriform nuclei. J Comp Neurol 525, 1499-1508.

White, M.G., Panicker, M., Mu, C., Carter, A.M., Roberts, B.M., Dharmasri, P.A., Mathur, B.N., 2018. Anterior Cingulate Cortex Input to the Claustrum Is Required for Top-Down Action Control. Cell Rep 22, 84-95.

Xiao, Q., Zhou, X., Wei, P., Xie, L., Han, Y., Wang, J., Cai, A., Xu, F., Tu, J., Wang, L., 2021. A new GABAergic somatostatin projection from the BNST onto accumbal parvalbumin neurons controls anxiety. Mol Psychiatry 26, 4719-4741.

Xu, J., Jo, A., DeVries, R.P., Deniz, S., Cherian, S., Sunmola, I., Song, X., Marshall, J.J., Gruner, K.A., Daigle, T.L., Contractor, A., Lerner, T.N., Zeng, H., Zhu, Y., 2022. Intersectional mapping of multi-transmitter neurons and other cell types in the brain. Cell Rep 40, 111036.

Yamagata, M., Sanes, J.R., 2018. Reporter-nanobody fusions (RANbodies) as versatile, small, sensitive immunohistochemical reagents. Proc Natl Acad Sci U S A 115, 2126-2131.

Yamauchi, K., Furuta, T., Okamoto, S., Takahashi, M., Koike, M., Hioki, H., 2022a. Protocol for multi-scale light microscopy/electron microscopy neuronal imaging in mouse brain tissue. STAR Protoc 3, 101508.

Yamauchi, K., Okamoto, S., Ishida, Y., Konno, K., Hoshino, K., Furuta, T., Takahashi, M., Koike, M., Isa, K., Watanabe, M., Isa, T., Hioki, H., 2022b. Fluorochromized tyramide-glucose oxidase as a multiplex fluorescent tyramide signal amplification system for histochemical analysis. Scientific Reports 12, 14807.

Yamauchi, K., Okamoto, S., Takahashi, M., Koike, M., Furuta, T., Hioki, H., 2022c. A Tissue Clearing Method for Neuronal Imaging from Mesoscopic to Microscopic Scales. J Vis Exp.

Zingg, B., Dong, H.W., Tao, H.W., Zhang, L.I., 2018. Input-output organization of the mouse claustrum. J Comp Neurol 526, 2428-2443.

Zufferey, R., Donello, J.E., Trono, D., Hope, T.J., 1999. Woodchuck hepatitis virus posttranscriptional regulatory element enhances expression of transgenes delivered by retroviral vectors. J Virol 73, 2886-2892.

Tables

Table 1. Colocalization of mRNA signals for VGluT1 or GAD67 with immunoreactivity for NeuN.

VGluT1 / NeuN			
	Core region	Shell region	
		Dorsal part	Ventral part
Rostral	93.2 ± 0.6[a] (7,928/8,513)[b]	90.2 ± 2.6 (6,737/7,443)	87.5 ± 5.1 (8,515/9,672)
Middle	90.8 ± 1.9 (4,065/4,460)	88.0 ±5.8 (5,654/6,321)	86.3 ± 5.3 (6,351/7,316)
Caudal	89.8 ± 0.7 (2,206/2,455)	91.1 ± 0.8 (5,778/6,329)	87.8 ± 2.5 (5,366/6,082)
Total	91.9 ± 0.7 (14,199/15,428)	91.4 ± 0.3 (18,169/20,093)	87.3 ± 4.3 (20,232/23,070)
GAD67 / NeuN			
	Core region	Shell region	
		Dorsal part	Ventral part
Rostral	8.7 ± 1.0[*] (637/7,046)	9.9 ± 0.2 (732/7,395)	10.9 ± 0.6 (1,227/11,370)
Middle	9.1 ± 2.2 (507/5,585)	9.4 ± 2.1 (554/5,932)	11.3 ± 3.1 (924/8,156)
Caudal	10.1 ± 1.1 (282/2,815)	8.3 ± 2.8 (451/5,564)	11.8 ± 2.0 (811/6,884)
Total	9.1 ± 1.2 (1,426/15,446)	9.3 ± 1.4 (1,737/18,891)	11.2 ± 1.4 (2,962/26,410)

[a]Data are provided as mean ± SD of the percentages in three mice.

[b]The denominator and numerator in parentheses correspond to the total number of cells immunoreactive for NeuN and that of neurons expressing VGluT1 or GAD67.

[*]$p = 0.0219$ versus the rostral part of the ventral shell region (Dunn's multiple comparison test after the Kruskal–Wallis test).

Table 2. Colocalization of immunoreactivity for PV, SOM, or VIP with mRNA signals for GAD67.

PV / GAD67			
	Core region	Shell region	
		Dorsal part	Ventral part
Rostral	28.5 ± 5.3[a, *] (310/1,036)[b]	15.4 ± 0.4 (129/835)	20.9 ± 3.0 (372/1,754)
Middle	23.4 ± 4.9 (164/703)	16.7 ± 0.8 (105/629)	18.2 ± 2.1 (191/1,057)
Caudal	23.1 ± 4.0 (75/315)	20.5 ± 0.8 (93/451)	20.3 ± 2.3 (179/883)
Total	26.2 ± 4.8 (549/2,054)	17.1 ± 0.1[†] (327/1,915)	20.0 ± 1.3 (742/3,694)
SOM / GAD67			
	Core region	Shell region	
		Dorsal part	Ventral part
Rostral	32.5 ± 1.0 (246/757)	28.4 ± 2.1 (294/1,034)	32.1 ± 1.1 (717/2,238)
Middle	30.0 ± 3.7 (259/860)	25.5 ± 5.2 (232/921)	32.3 ± 1.7 (448/1,384)
Caudal	26.6 ± 3.9 (139/515)	26.4 ± 1.3 (217/819)	32.0 ± 3.2 (372/1,166)
Total	30.2 ± 2.3 (644/2,132)	26.9 ± 2.8 (743/2,774)	32.1 ± 0.9 (1,537/4,788)
VIP / GAD67			
	Core region	Shell region	
		Dorsal part	Ventral part
Rostral	8.1 ± 1.0 (57/699)	11.3 ± 1.4 (92/825)	8.2 ± 1.6 (112/1,434)
Middle	10.4 ± 3.5 (62/584)	9.6 ± 2.2 (63/663)	8.8 ± 2.6 (95/1,027)
Caudal	9.6 ± 2.5 (32/341)	7.6 ± 0.8 (39/514)	9.6 ± 0.9 (74/776)
Total	9.3 ± 1.3 (151/1,624)	9.7 ± 0.2 (194/2,002)	8.7 ± 1.5 (281/3,237)

[a]Data are provided as mean ± SD of the percentages in three mice.

[b]The denominator and numerator in parentheses correspond to the total number of neurons expressing GAD67 mRNA and that of neurons immunoreactive for PV, SOM, or VIP.

[*]$p = 0.0219$ versus the rostral part of the core region and 0.0219 versus the caudal part of the dorsal shell region (Dunn's multiple comparison test after the Kruskal–Wallis test).

[†]$p = 0.0219$ versus the total core region (Dunn's multiple comparison test after the Kruskal–Wallis test).

Table 3. Colocalization of immunoreactivities for PV, SOM, and VIP.

	Core region	Shell region	
		Dorsal part	Ventral part
PV / SOM	3.0 ± 1.1[a] (8/279)[b]	1.1 ± 0.9 (3/274)	0.5 ± 0.5 (3/604)
SOM / PV	3.0 ± 0.6 (8/269)	1.4 ± 1.2 (3/204)	0.8 ± 0.8 (3/394)
SOM / VIP	0 (0/65)	0 (0/65)	0.9 ± 1.6 (1/96)
VIP / SOM	0 (0/279)	0 (0/274)	0.2 ± 0.3 (1/604)
VIP / PV	0 (0/269)	0 (0/204)	0 (0/394)
PV / VIP	0 (0/65)	0 (0/65)	0 (0/96)

[a]Data are provided as mean ± SD of the percentages in three mice.

[b]The denominator and numerator in parentheses correspond to the total number of the neurons immunoreactive for PV, SOM, or VIP.

Table 4. Dendritic and axonal lengths of three-dimensionally reconstructed PV and SOM neurons in the claustral core and shell regions.

Dendritic length

	PV-core	SOM-core	PV-shell	SOM-shell
Inside claustrum	99.1 ± 0.8[a] (8,424 ± 866)[b]	95.7 ± 7.5 (4,874 ± 853)	79.0 ± 13.5 (6,502 ± 1,027)	74.7 ± 19.6 (3,365 ± 1,021)
Core region	76.0 ± 5.5 (6,459 ± 757)	79.4 ± 13.9 (3,996 ± 530)	3.9 ± 2.4 (311 ± 164)	2.5 ± 2.7 (99 ± 85)
Shell region	23.0 ± 5.2 (1,965 ± 532)	16.3 ± 9.5 (878 ± 573)	75.1 ± 14.8 (6,190 ± 1,162)	72.5 ± 19.1 (3,267 ± 1,038)
Outside claustrum	0.9 ± 0.8 (83 ± 72)	4.3 ± 7.5 (292 ± 506)	21.0 ± 13.5 (1,845 ± 1,448)	25.0 ± 19.6 (1,140 ± 967)
Total	(8,507 ± 938)	(5,165 ± 1,355)	(8,347 ± 1,668)	(4,505 ± 718)

Axonal length

	PV-core	SOM-core	PV-shell	SOM-shell
Inside claustrum	99.8 ± 0.3 (71,070 ± 11,218)	94.6 ± 9.3 (61,941 ± 21,548)	85.7 ± 12.5 (56,219 ± 17,344)	64.8 ± 25.9 (56,873 ± 28,584)
Core region	92.8 ± 6.1 (65,931 ± 10,354)	84.4 ± 10.5 (55,263 ± 20,367)	12.1 ± 5.0 (7,797 ± 2,996)	7.3 ± 3.8 (6,315 ± 3,644)
Shell region	7.0 ± 5.8 (5,138 ± 4,220)	10.2 ± 7.9 (6,677 ± 6,006)	73.6 ± 11.8 (48,422 ± 16,268)	57.6 ± 24.3 (50,557 ± 26,880)
Outside claustrum	0.2 ± 0.3 (125 ± 196)	5.4 ± 9.3 (2,392 ± 4,140)	14.3 ± 12.5 (8,859 ± 7,428)	35.2 ± 25.9 (32,301 ± 29,421)
Total	(71,195 ± 11,232)	(64,333 ± 17,463)	(65,078 ± 14,128)	(89,173 ± 34,162)

[a]Data are provided as mean ± SD of the percentages in three to five reconstructed neurons.

[b]Lengths (μm) of the dendrites and axons are provided as mean ± SD in three to five reconstructed neurons.

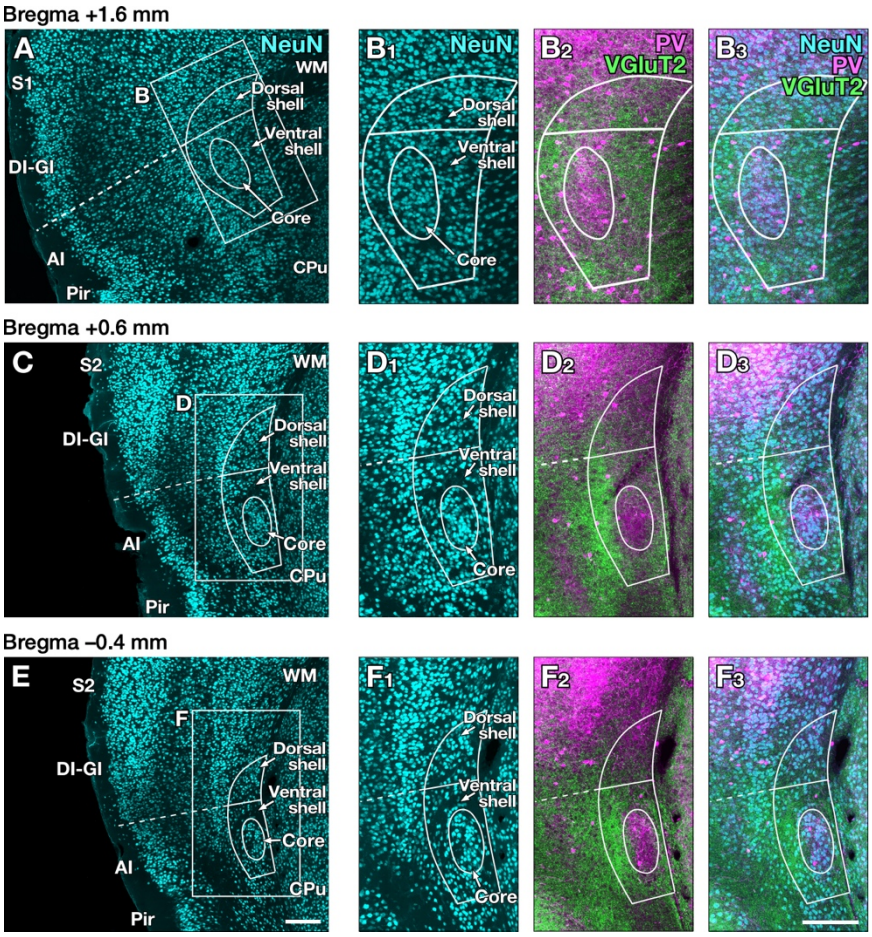

Figure 1. Delineation of the mouse claustral subregions based on cytoarchitecture.

(**A–F**) Triple immunofluorescence labeling for NeuN (AF488), PV (AF568), and VGluT2 (AF647) on mouse coronal sections at 1.6 mm rostral (A, B), 0.6 mm rostral (C, D), and 0.4 mm caudal (E, F) to the bregma. The subregions of the claustrum were identified according to immunoreactivity for NeuN (A, C, E): core region and dorsal and ventral shell regions. The core and shell regions showed high and low density of neuronal cells (B_1, B_3, D_1, D_3, F_1, F_3) and corresponded to the area displaying strong immunoreactivity for PV or VGluT2, respectively (B_2, B_3, D_2, D_3, F_2, F_3). Dashed lines indicate the border between the DI and AI, and the extended lines of the border subdivided the shell regions into the dorsal and ventral parts (A, C, D). CPu, caudate-putamen; GI, granular insular cortex; Pir, piriform cortex; S1, primary somatosensory cortex; S2, secondary somatosensory cortex; WM, white matter. Scale bar = 200 μm in (E) applies to (A, C), 200 μm in (F_3) applies to (B_1–B_3, D_1–D_3, F_1–F_2)

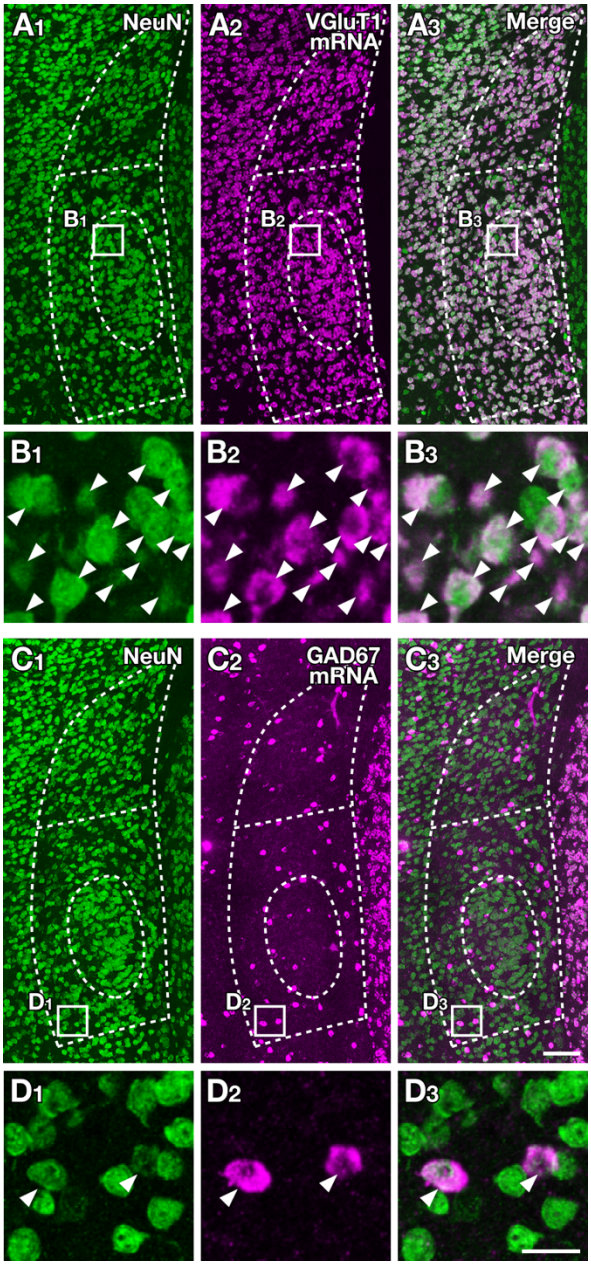

Figure 2. VGluT1- and GAD67-expressing neuronal cells in the mouse claustrum.

(**A_1–D_3**) Combination of immunofluorescence histochemistry for NeuN (AF488) and fluorescence in situ hybridization histochemistry for VGluT1 or GAD67 mRNA (AF647). The distributions of VGluT1- and GAD67-expressing cells were quantified by counting the total number of cells immunoreactive for NeuN and that of cells expressing VGluT1 or GAD67 mRNA (arrowheads; B_1–B_3, D_1–D_3) in each claustral subregion. Scale bar = 100 μm in (C_3) applies to (A_1–A_3, C_1–C_2), 25 μm in (D_3) applies to (B_1–B_3, D_1–D_2).

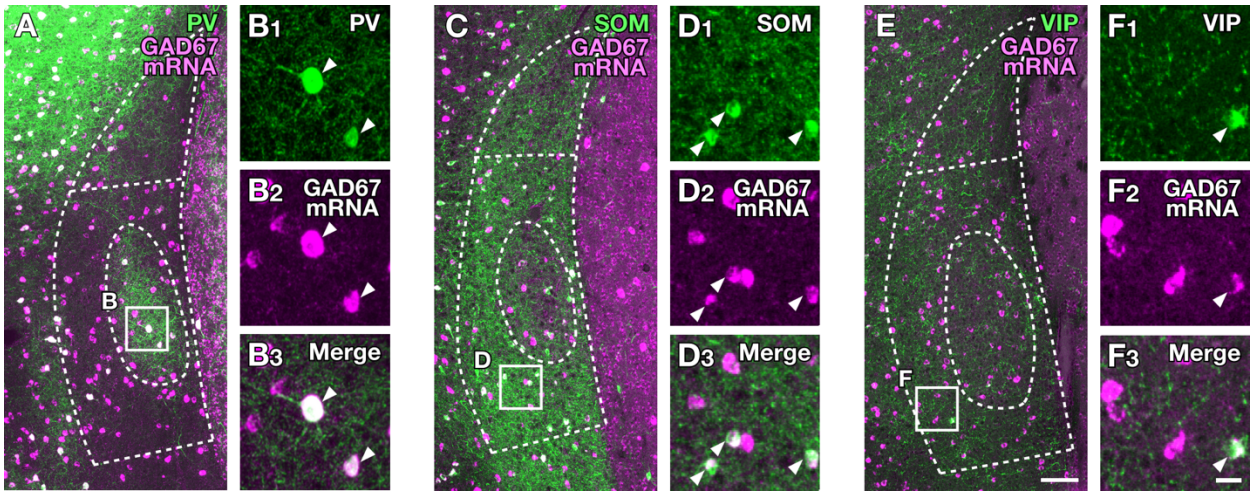

Figure 3. PV, SOM, and VIP immunoreactivities in claustral GABAergic neurons.

(**A–F$_3$**) Immunoreactivities for NeuN and one of the markers (PV, SOM, or VIP) and signals for GAD67 mRNA were visualized with AF488 (not shown), AF568 (green), and AF647 (magenta). Almost all cells immunoreactive for PV, SOM, or VIP displayed signals for GAD67 mRNA. The distributions of GABAergic neuron subgroups were quantified by counting the total number of cells expressing GAD67 mRNA and that of neuronal cells immunoreactive for PV (A, B$_1$–B$_3$), SOM (C, D$_1$–D$_3$), or VIP (E, F$_1$–F$_3$) in each claustral subregion (arrowheads). Scale bar = 100 μm in (E) applies to (A, C), 25 μm in (F$_3$) applies to (B$_1$–B$_3$, D$_1$–D$_3$, F$_1$–F$_2$).

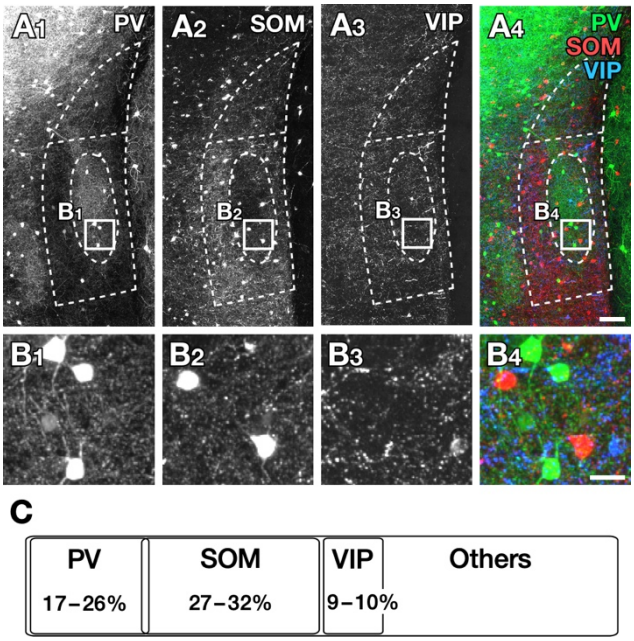

Figure 4. Three distinct subgroups of PV-, SOM-, or VIP-immunoreactive GABAergic neurons in the mouse claustrum.

(**A_1–B_4**) Quadruple immunofluorescence labeling for NeuN (CF405M; not shown), PV (AF488), SOM (AF568), and VIP (Cy5). Almost no colocalization of immunoreactivity was found in the claustrum. (**C**) Venn diagram summarizing the relative population sizes of GABAergic neurons in the claustrum. PV, SOM, and VIP constituted approximately 60% of GABAergic neurons in each claustral subregion. Scale bar = 100 μm in (A_4) applies to (A_1–A_3), 25 μm in (B_4) applies to (B_1–B_3).

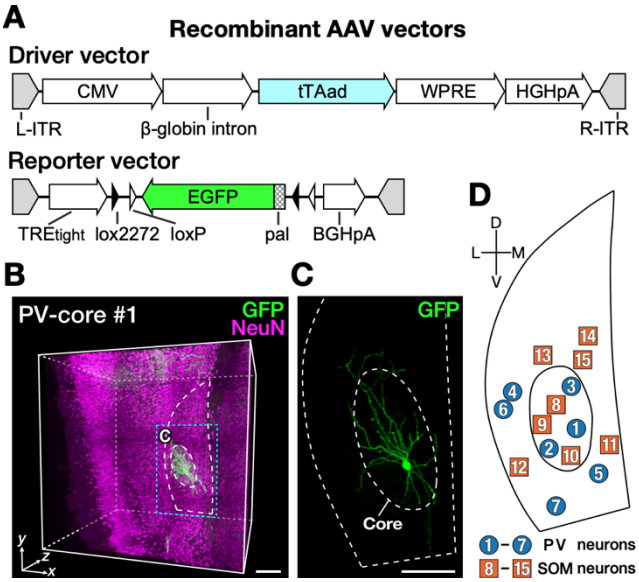

Figure 5. Visualization of PV and SOM neurons in the claustral core and shell regions.

(**A**) The driver vector (AAV2/1-CMV-tTA-WPRE) and the reporter vector (AAV2/1-TRE-FLEX-palGFP-BGHpA). The driver vector expresses tTAad with cytomegalovirus (CMV) promoter, while the reporter vector produces a reporter protein, membrane-targeted EGFP (palGFP), under the control of a TRE_{tight} in the presence of Cre recombinase. The mixture of the diluted driver (8.0×10^8 gc/mL) and undiluted reporter vectors (4.4×10^{14} gc/mL) was injected into the claustrum of $PV^{+/Cre}$ or $SOM^{+/Cre}$ mice. (**B**) 3D volume rendering of a 1-mm-thick coronal slice with immunofluorescence labeling for GFP and NeuN. After optical clearing, the 3D image stacks of the slice were acquired with an SDCM. White dot lines indicate the claustrum and its core region. (**C**) A higher magnification image of the rectangle in (B). The cell body of a PV neuron was located in the core region. (**D**) Seven PV neurons (#1–7 within blue circles) and eight SOM neurons (#8–15 within orange squares) in the claustral core and ventral shell regions were analyzed in this study. #4, 9, 10, 11, and 14 neurons were derived from male mice; #1, 2, 3, 5, 6, 7, 8, 12, 13, and 15 neurons from female mice. The locations of their cell bodies were projected onto a coronal section of the claustrum. BGHpA, polyadenylation signal derived from the bovine growth hormone gene; HGHpA, polyadenylation signal derived from the human growth hormone gene; ITR, inverted terminal repeat; pal, palmitoylation signal derived from the GAP-43 N-terminus. Scale bar = 200 μm in (B), 100 μm in (C).

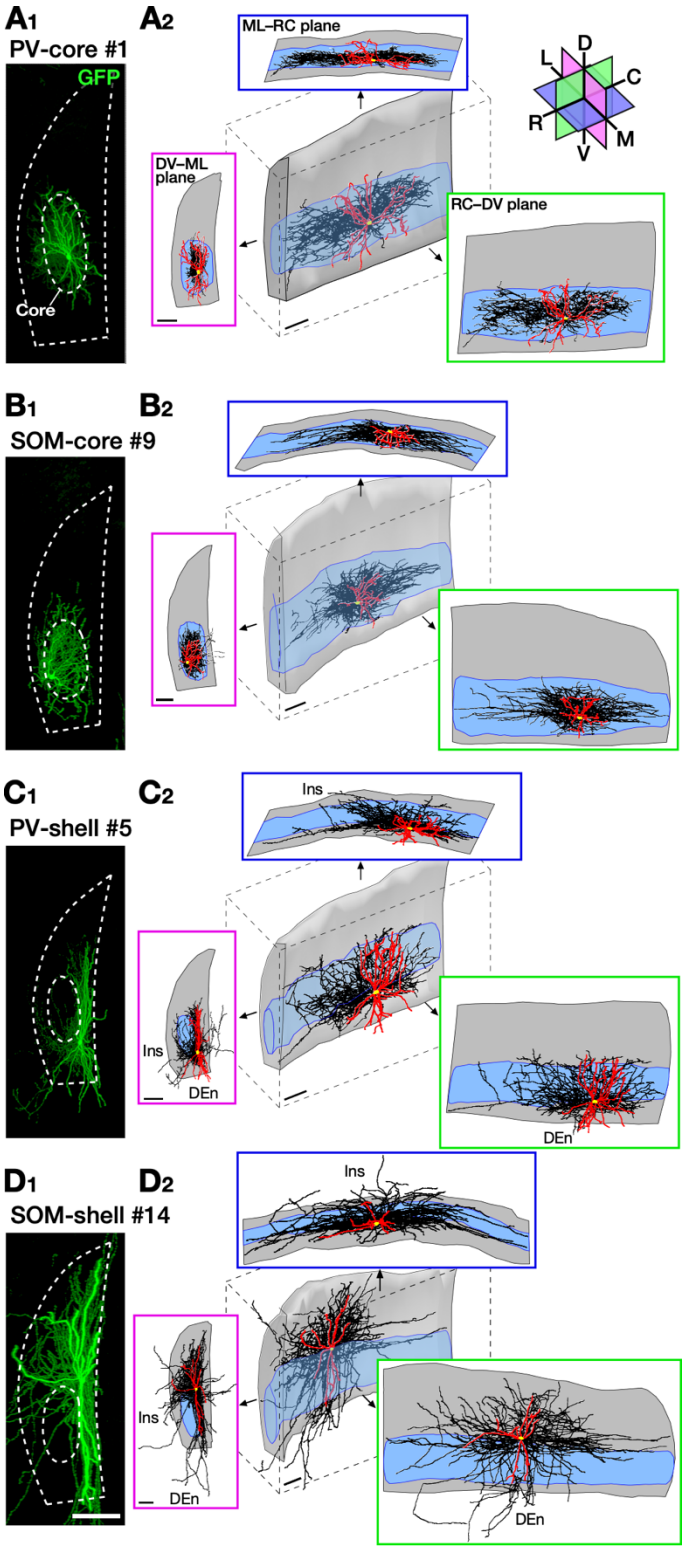

Figure 6. 3D reconstruction of PV and SOM neurons in the claustral core and shell regions.

(**A$_1$**) PV neuron in the core region (PV-core #1). White dot lines indicate the claustrum and its core region. (**A$_2$**) 3D reconstruction of PV-core #1 neuron. After 3D reconstruction, the dendritic and axonal arborizations were projected onto the plane along the RC, DV, or ML axis (indicated as "DV–ML plane," "ML–RC plane," or "RC–DV plane" in the inset with magenta, blue, or green square, respectively). Cell bodies, dendrites, and axons are shown in yellow circles, red lines, and black lines. The core and shell regions are indicated in cyan and gray, respectively. (**B$_1$–D$_2$**) SOM neuron in the core region (SOM-core #9; B$_1$, B$_2$), PV neuron in the ventral

shell region (PV-shell #5; C_1, C_2), and SOM neuron in the ventral shell region (SOM-shell #14; D_1, D_2). Ins, insular cortex. Scale bar = 150 μm in (D_1) applies to (A_1–C_1), 150 μm in (A_2–D_2).

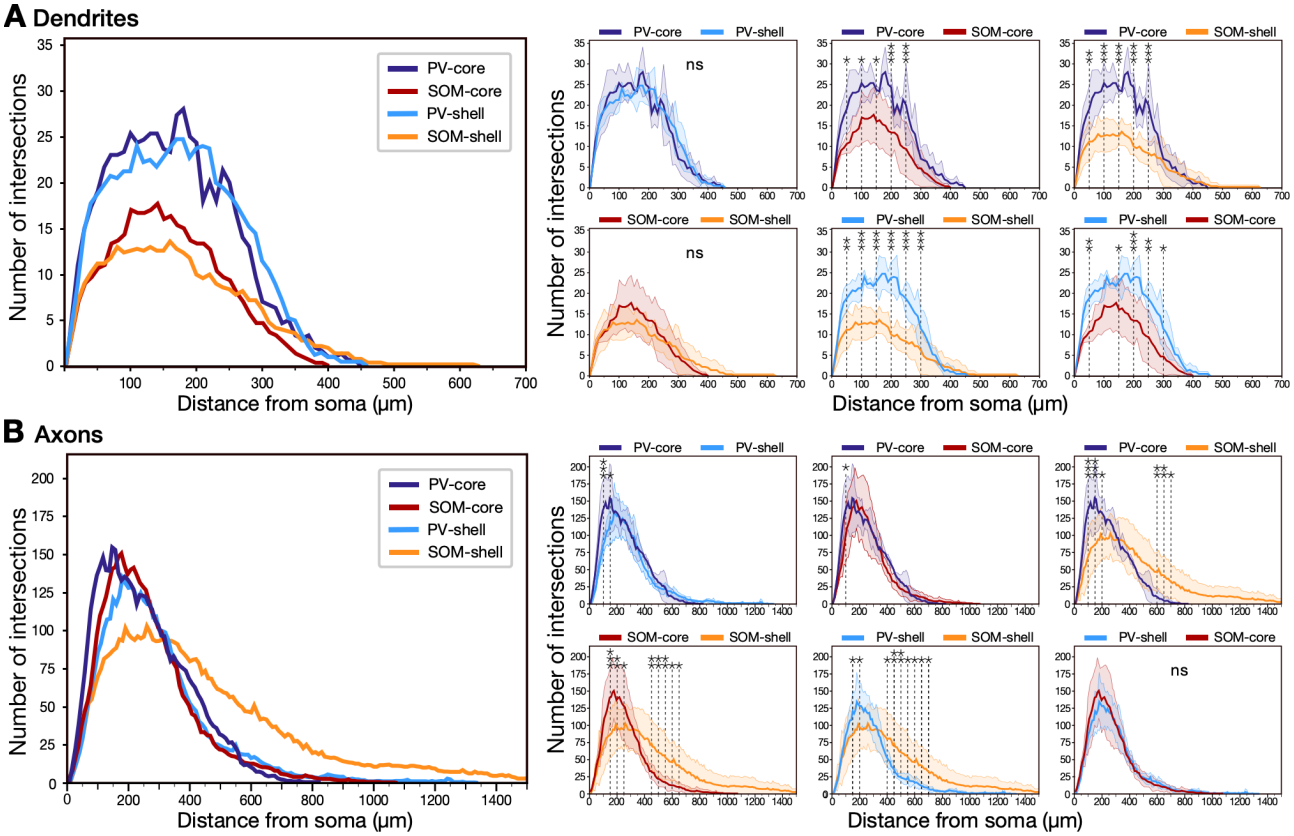

Figure 7. 3D Sholl analysis for the dendrites and axons of PV and SOM neurons in the claustral core and shell regions.

(**A**) 3D Sholl analysis for the dendrites of PV and SOM neurons in the core and shell regions. The mean numbers of dendritic intersections were plotted against the radial distance of concentric spheres from the soma (left). Multiple statistical comparison was performed among PV-core, PV-shell, SOM-core, and SOM-shell neurons in every 50 μm from the soma with two-way ANOVA followed by post-hoc Bonferroni's multiple comparison test (ns, not significant, $^{*}p < 0.05$, $^{**}p < 0.01$, and $^{***}p < 0.001$; right). The mean number of intersections (solid line) and its SD (shaded area) of PV-core, PV-shell, SOM-core, and SOM-shell neurons are shown in blue, pale blue, red, and orange, respectively. (**B**) 3D Sholl analysis for the axons of PV and SOM neurons in the core and shell regions (left). Multiple statistical comparison was performed among PV-core, PV-shell, SOM-core, and SOM-shell neurons in every 50 μm from the soma with two-way ANOVA followed by post-hoc Bonferroni's multiple comparison test (ns, not significant, $^{*}p < 0.05$, $^{**}p < 0.01$, and $^{***}p < 0.001$; right).

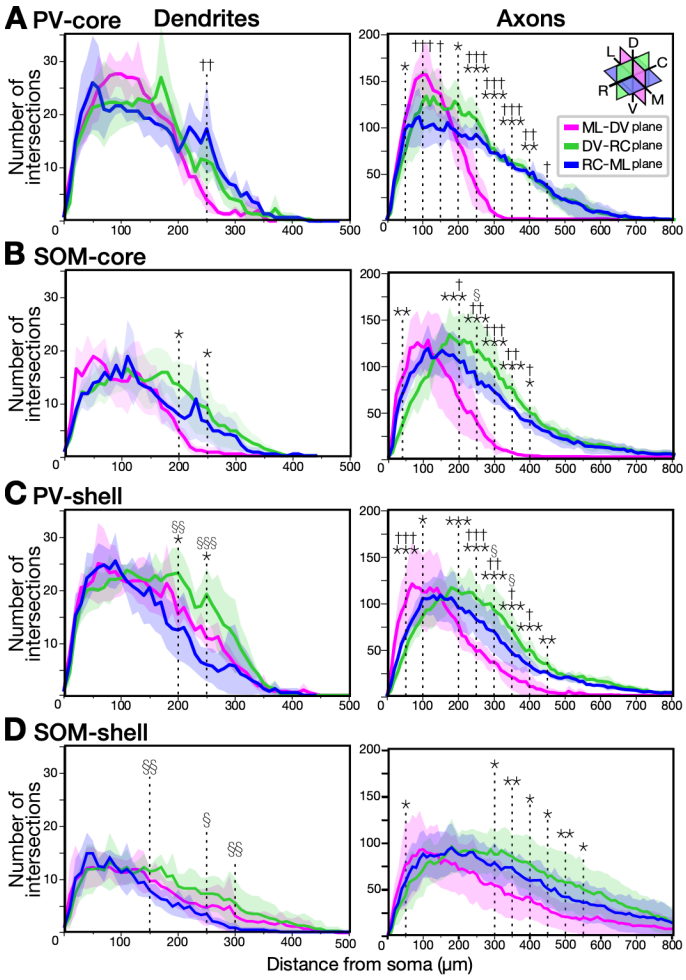

Figure 8. 2D Sholl analysis for the dendrites and axons of PV and SOM neurons in the claustral core and shell regions.

(**A–D**) 2D Sholl analysis for the dendrites and axons of PV-core (A), SOM-core (B), PV-shell (C), and SOM-shell (D) neurons. The reconstructed data were projected onto the plane perpendicular to either the RC, ML, or DV axis (ML–DV, DV–RC, or RC–ML plane). The mean number of dendritic or axonal intersections on each ML–DV, DV–RC, or RC–ML plane was plotted against the radial distance of concentric circles from the soma. Multiple statistical comparisons for dendrites or axons of each neuronal type were performed among the numbers of intersections on the ML–DV, DV–RC, and RC–ML planes in every 50 μm from the soma with two-way ANOVA followed by post-hoc Bonferroni's multiple comparison test ($^{*}p < 0.05$, $^{**}p < 0.01$, and $^{***}p < 0.001$ between the ML–DV and DV–RC planes; $^{\dagger}p < 0.05$, $^{\dagger\dagger}p < 0.01$, and $^{\dagger\dagger\dagger}p < 0.001$ between the ML–DV and RC–ML planes; $^{\S}p < 0.05$, $^{\S\S}p < 0.01$, and $^{\S\S\S}p < 0.001$ between the DV–RC and RC–ML planes). The mean number of intersections (solid line) and its SD (shaded area) on the ML–DV, RC–ML, or DV–RC plane are shown in magenta, green, or blue, respectively. The axonal ramifications of these neurons on the ML–DV plane were skewed to the closer areas from the soma than those on the DV–RC and RC–ML planes.

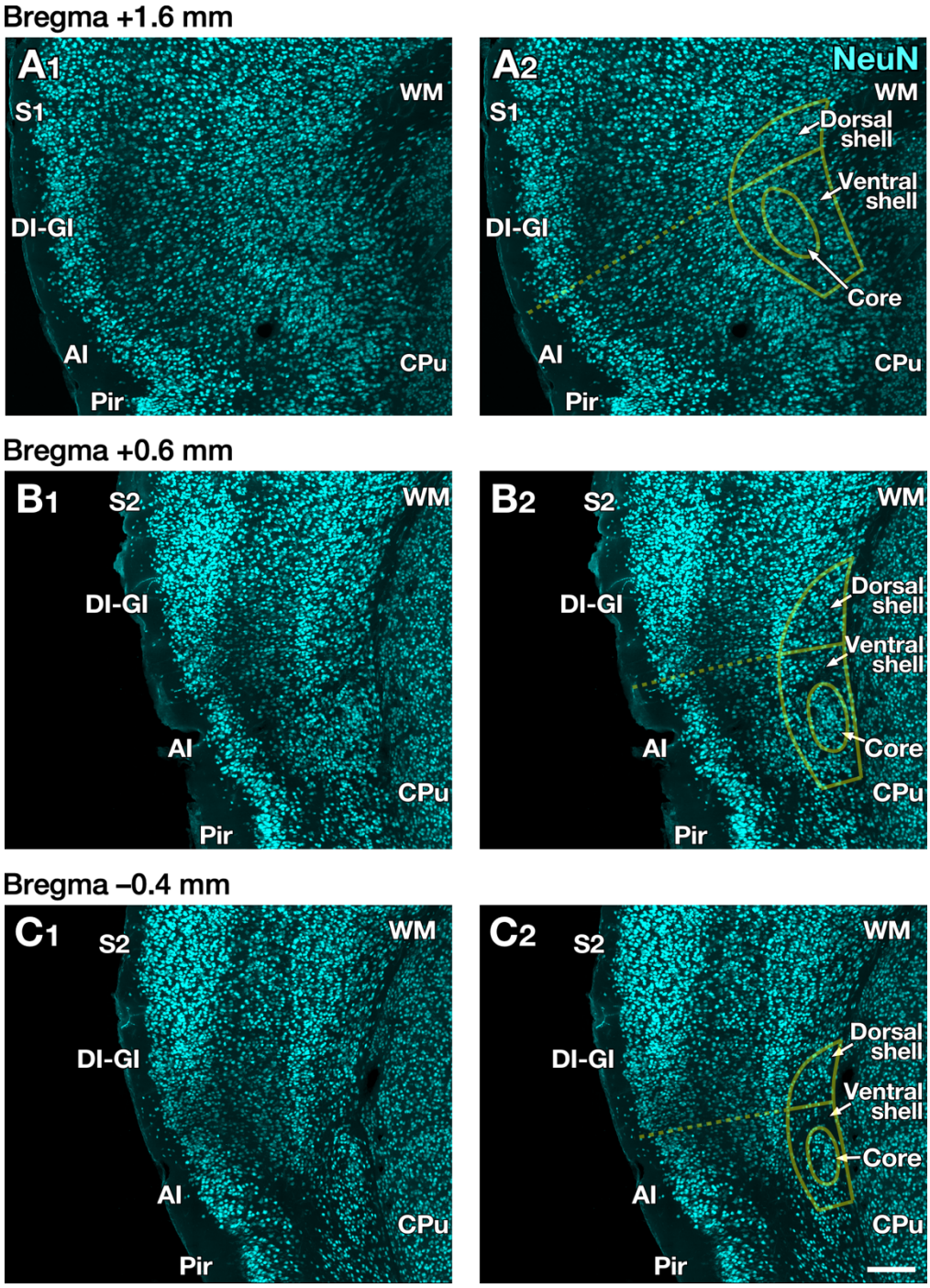

Supplementary Figure S1. Delineation of the mouse claustral subregions based on cytoarchitecture. (**A–C**) The immunofluorescence images for NeuN on mouse coronal sections, shown in Fig. 1, at 1.6 mm rostral (A), 0.6 mm rostral (B), and 0.4 mm caudal (C) to the bregma. Based on cytoarchitecture (A_1, B_1, C_1), the claustral subregions were delineated (yellow lines; A_2, B_2, C_2). CPu, caudate-putamen; GI, granular insular cortex; Pir, piriform cortex; S1, primary somatosensory cortex; S2, secondary somatosensory cortex; WM, white matter. Scale bar = 200 μm in (C_2) applies to (A_1, A_2, B_1, B_2, C_1).

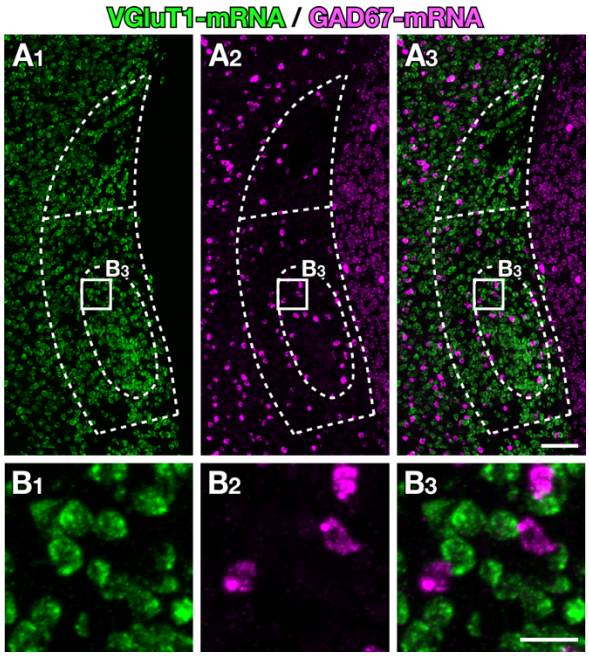

Supplementary Figure S2. No colocalization of the signals for VGluT1 and GAD67 mRNAs.

(**A**–**B**) Combination of fluorescence in situ hybridization histochemistry for VGluT1 (CF488; green) and GAD67 mRNAs (CF568; magenta) with immunofluorescence histochemistry for NeuN (not shown). The numbers of cells expressing VGluT1 and GAD67 mRNAs were counted in each claustral subregion from three mice: 1105, 942, and 1437 of VGluT1-expressing cells, and 100, 81, and 163 of GAD67-expressing cells in the core, dorsal shell, and ventral shell regions, respectively. No colocalization of the signals for VGluT1 and GAD67 mRNAs was found throughout the claustrum. Scale bar = 100 μm in (A_3) applies to (A_1, A_2), 25 μm in (B_3) applies to (B_1, B_2).

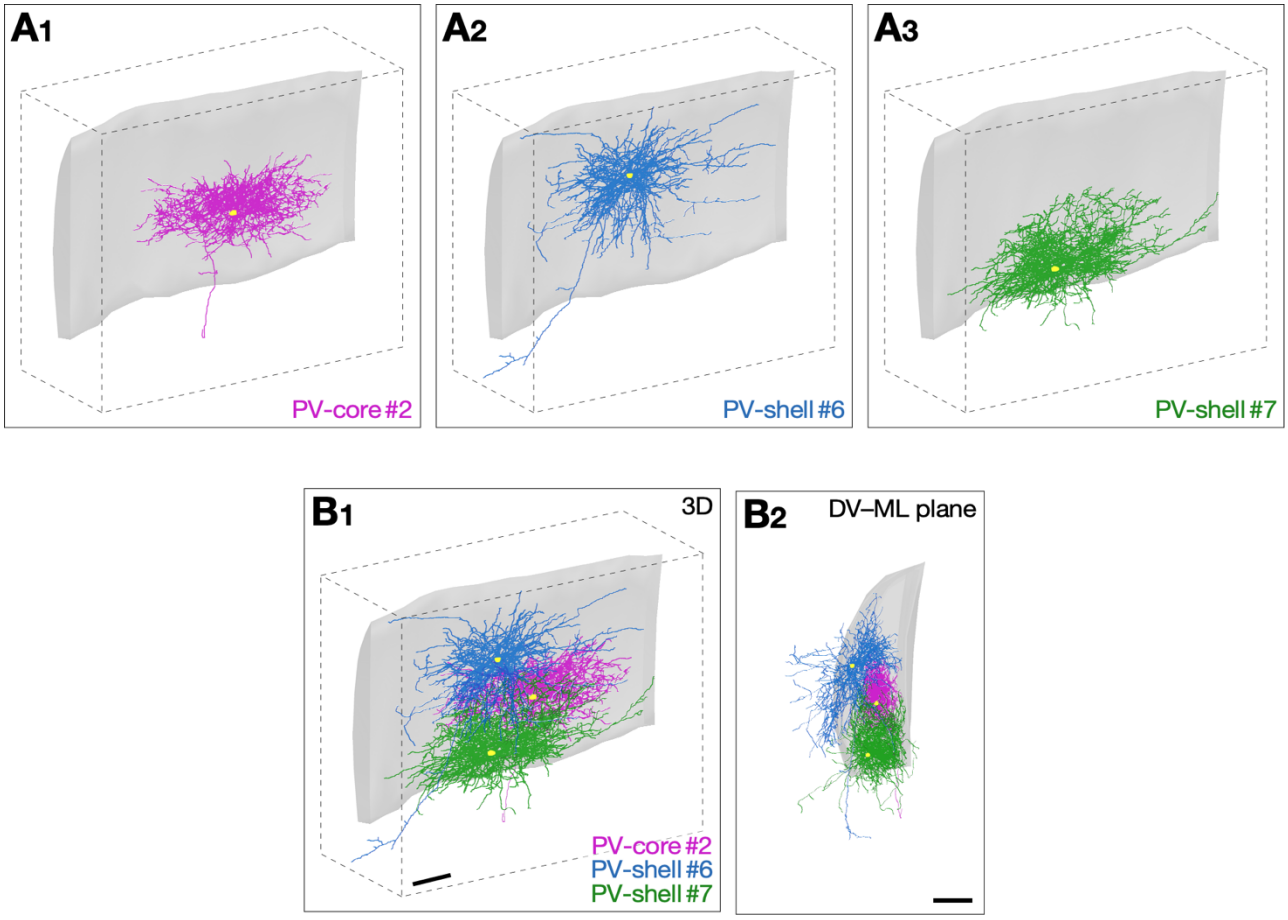

Supplementary Figure S3. 3D reconstructions of PV-core #2, PV-shell #6, and PV-shell #7 neurons in a single hemisphere.

(**A–B**) PV-core #2 (A_1; magenta), PV-shell #6 (A_2; blue), and PV-shell #7 (A_3; green) neurons were reconstructed from a single hemisphere (B_1). Because the neurites of the three neurons had few overlaps (B_2), the neurites of each neuron were separated from neighboring labeled neurons. The dendrites and axons of PV-core #2, PV-shell #6, and PV-shell #7 neurons are shown in magenta, blue, and green, respectively. The claustral regions and neuronal cell bodies are shown in gray and yellow. Scale bar = 150 μm in (B_1) applies to (A_1–A_3), 150 μm in (B_2).

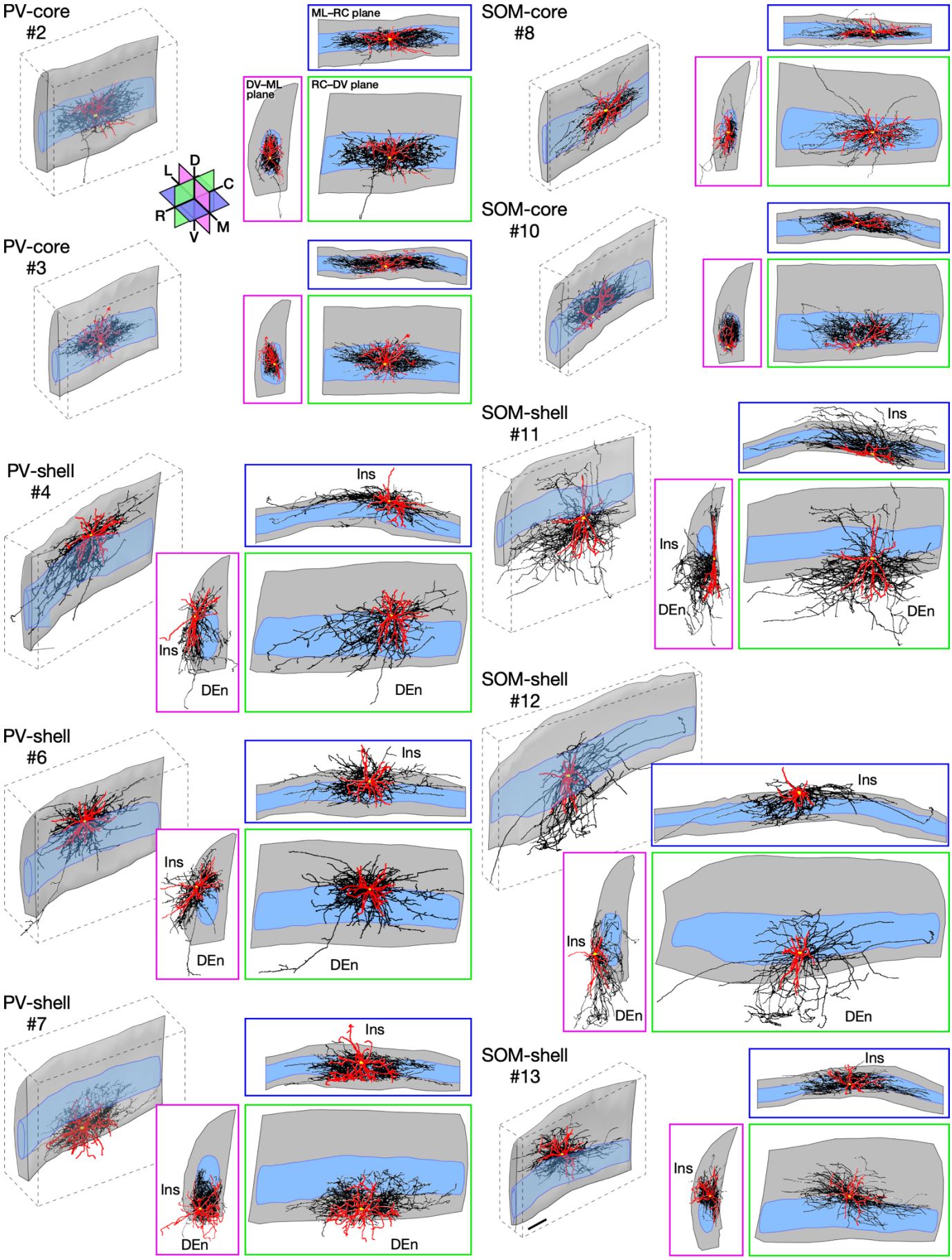

Supplementary Figure S4. (*Continued on next page*)

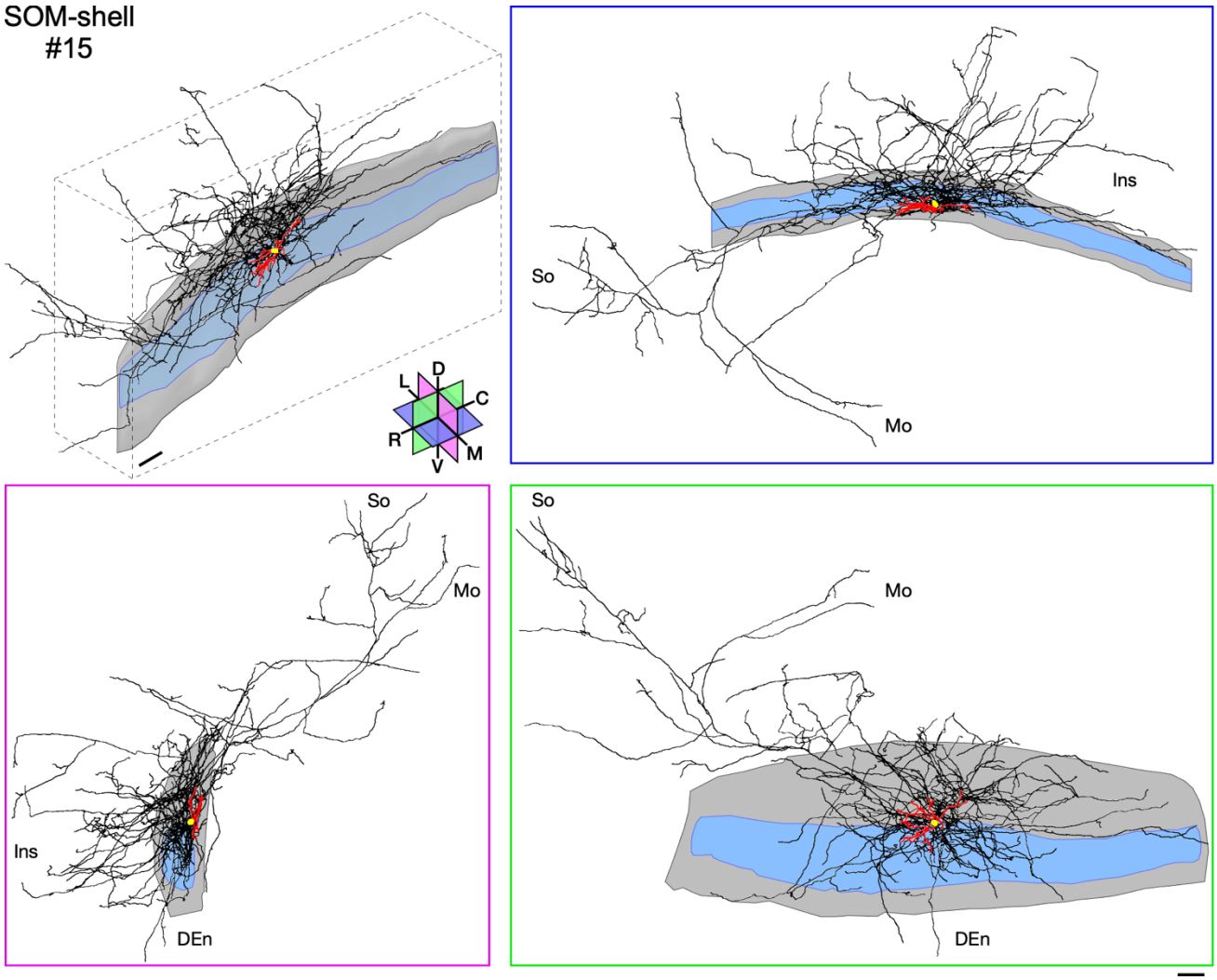

Supplementary Figure S4. 3D reconstruction of PV and SOM neurons in the claustral core and shell regions.

3D reconstructions of PV-core neurons (#2, 3), SOM-core neurons (#8, 10), PV-shell neurons (#4, 6, 7), and SOM-shell neurons (#11, 12, 13, 15). After 3D reconstruction, the dendritic and axonal arborizations were projected onto the plane along the RC, DV, or ML axis (indicated as "DV–ML plane," "ML–RC plane," or "RC–DV plane" in the inset with magenta, blue, or green square, respectively). Cell bodies, dendrites, and axons are shown in yellow circles, red lines, and black lines, respectively. The core and shell regions are indicated in cyan and gray, respectively. Ins, insular cortex; Mo, motor cortex; So, somatosensory cortex. Scale bar = 150 μm.

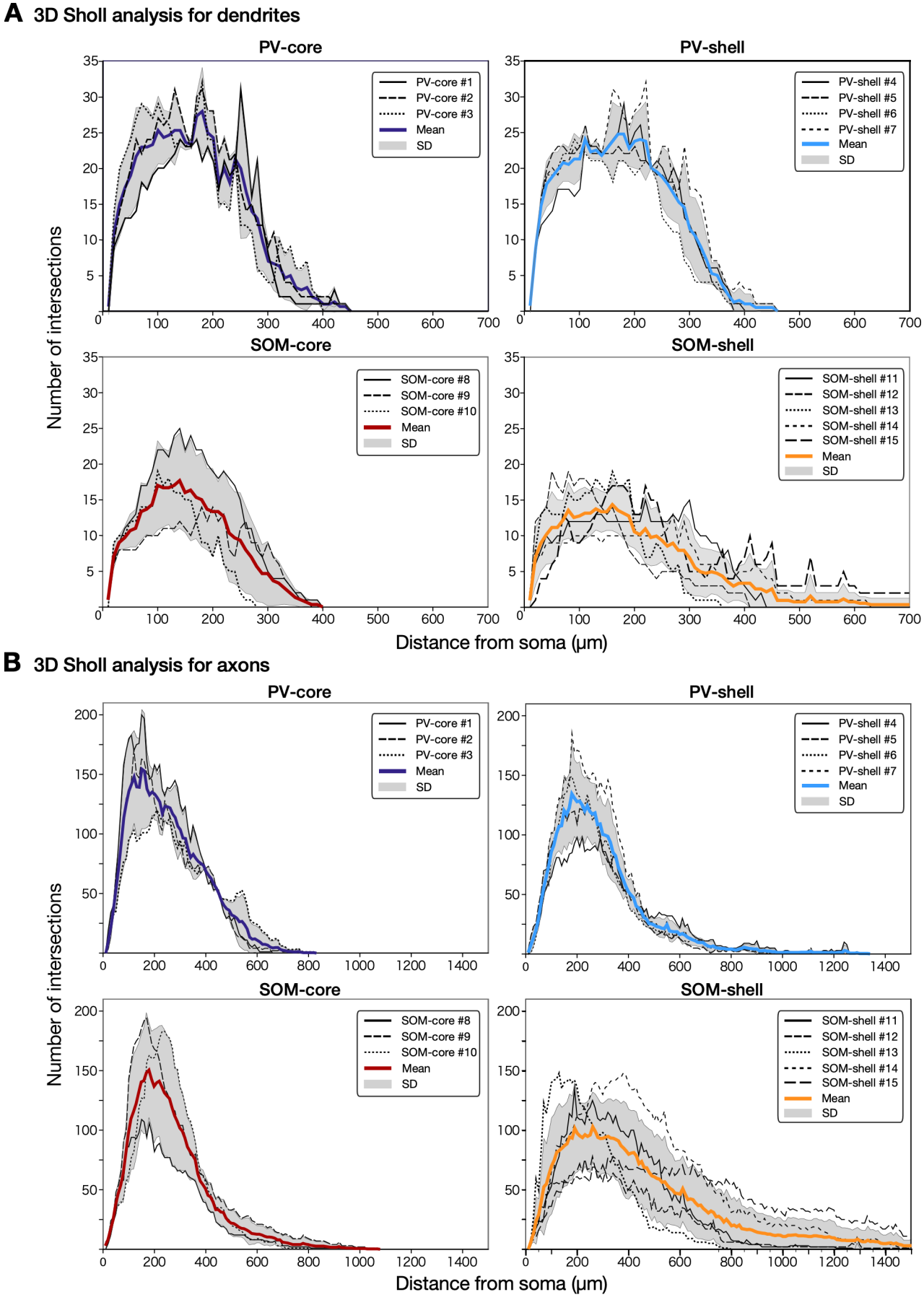

Supplementary Figure S5. (*Legend on next page*)

Supplementary Figure S5. 3D Sholl analysis for the dendrites and axons of individual PV and SOM neurons in the claustral core or shell region.

(**A**) 3D Sholl analysis for the dendrites of individual PV and SOM neurons in the core and shell regions. Broken lines show the number of intersections in individual neurons, while solid lines and gray shaded areas indicate the mean value and SD. (**B**) 3D Sholl analysis for the axons of individual PV and SOM neurons in the core and shell regions.

Supplementary Table. Primers and oligonucleotides used in the present study.

P1	5′-CGCGGGTACC-3′
P2	5′-TCGAGGATATCACGCGTA-3′
P3	5′-GATCTACGCGTGATATCC-3′
P4	5′-AAAAACGCGTCGATAATCAACCTCTGGATT-3′
P5	5′-TTTTAGATCTCGATGCGGGGAGGCGGCCCA-3′
P6	5′-AAAAGGATCC**GCCACC**ATGTCTAGACTGGA-3′
P7	5′-TTTTGTCGACTTACCCGGGGAGCATGTCAA-3′
P8	5′-AATTGGATCCAGATCTGTCGACA-3′
P9	5′-CGCGTGTCGACAGATCTGGATCC-3′
P10	5′-GATCGTACGT-3′
P11	5′-AATTCGGCAGATCTAGCGTCGACGGCAAGCTTAGCGGATCCGGCTGATCTC-3′
P12	5’-TCGAGAGATCAGCCGGATCCGCTAAGCTTGCCGTCGACGCTAGATCTGCCG-3′
P13	5′-AAAAGGATCC**GCCACC**ATGCTGTGCTGTAT-3′
P14	5′-TTTTGTCGACTTACTTGTACAGCTCGTCCA-3′
P15	5′-GGAACCCCTAGTGATGGAGTT-3′
P16	5′-CGGCCTCAGTGAGCGA-3′

Bold characters indicate the Kozak consensus sequence. Underlined sequences indicate the restriction sites for BamHI in P6, P8, P9, P11, P12, and P13; BglII in P5, P8, P9, P11, and P12; EcoRV in P2 and P3; HindIII in P11 and P12; KpnI in P1; MluI in P2, P3, and P4; and SalI in P7, P8, P9, P11, P12, and P14.